5-14-2010

Time-Lapse Depletion Modeling Sensitivity Study: Gas-Filled Gulf of Mexico Reservoir

Christy Gautre
University of New Orleans

Time-Lapse Depletion Modeling Sensitivity Study: Gas-Filled Gulf of Mexico Reservoir

A Thesis

Submitted to the Graduate Faculty of the
University of New Orleans
in partial fulfillment of the
requirements for the degree of

Master of Science
in
Applied Physics

by

Christy Finch Gautre

B.S. Centenary College of Louisiana, 2002

May, 2010

Acknowledgements

I would first most like to thank Mark Mannion for advising me throughout this entire thesis project, from beginning to end. He truly has been a great mentor, and has demonstrated patience and kindness, and gave much insight to the project. I will greatly miss him as he enters the next stage of his life- retirement.

Next, I would like to thank my advisors Dr. Juliette Ioup and Dr. George Ioup for giving me the freedom to develop my thesis project, and for all of their assistance. Additionally, Dr. Juliette Ioup and Dr. George Ioup have been wonderful advisors throughout my graduate studies as they have worked dutifully to help me with my studies while I have been a part-time student, and full-time worker. Without their support, I would have thought completing my studies would be impossible.

Next, I would like to thank my colleagues Tin-Wai Lee, Hao Zhou, and Chuck Collins for their help on various aspects of this project. Also, I could not have completed the project without the data provided by Anastasia Minaeva and Mosab Nasser.

I would also like to thank my husband, T.J. Gautre, for his support as I have completed my graduate studies. It has been a tough road, but now it will be exciting to see where the next turn on this road will take us. I am looking forward to traveling that road with you!

Table of Contents

List of Figures

List of Tables

Abstract

Time-lapse seismic allows oil/gas reservoir monitoring during production, highlighting compaction and water movement. Time-lapse modeling, using a stress-dependent rock physics model, helps determine the need and frequency of expensive repeat seismic acquisition. We simulate a Gulf of Mexico gas reservoir time-lapse response for depletion and water flooding using uncertainty ranges in water saturation, porosity, stress-induced velocity changes, and pore compressibility.

An analysis is conducted to see if a water-swept region could have been predicted. Findings show the swept and un-swept monitor cases amplitude differences range from 6% to 15%, which is higher than the actual monitor seismic noise level. Thus, it is unlikely these cases could be differentiated.

However, the modeled amplitude changes from base to monitor cases do not match measured amplitude changes. This suggests the rock property model requires pressure-variance improvement and/or the changes in seismic amplitudes are associated with pressure/porosity, thickness, or saturation cases not modeled.

Keywords: gas, oil, reservoir, time-lapse seismic, rock physics modeling, depletion, water flood, production, Gulf of Mexico, 4D

Introduction

As oil or gas is removed from a reservoir, the reservoir can experience water movement and/or compaction. These changes in the reservoir alter the reservoir's acoustic response. Time-lapse (4D) reservoir imaging via repeat seismic surveys provides data that show the evolving seismic signature due to water movement and compaction. Time-lapse reservoir imaging is important because it can help determine reservoir connectivity and fluid flow patterns and increase recovery rates (Fanchi, 2001). As 4D seismic analysis can show water movement over time, drilling costly dry holes can potentially be avoided.

Time-lapse acoustic reservoir modeling studies, or 4D feasibility studies, are conducted to determine if expected changes in a reservoir would produce measurable changes in seismic data. These modeling studies rely heavily on a robust, stress-dependent rock physics model that accurately predicts acoustic changes in the reservoir due to compaction and water movement. For instance, Herwanger et al. (2009) use dynamic reservoir modeling and geomechanical modeling to explain time lapse seismic signals, and conclude that time lapse seismic has the potential to be used to determine stress paths. Tura et al. (2006) predict that a 4D response would dominate seismic noise for a producing gas reservoir in South America noting, however, that the expected stress-induced velocity response should be updated as new core data are collected.

Time-lapse seismic data can also be used to build and improve dynamic reservoir models. Castro et al. (2009) use two methods to incorporate 4D seismic data into reservoir modeling workflows, where the second uses 4D seismic data with a clear time-lapse signal paired with production data to improve a reservoir model for a reservoir in the Norwegian North Sea.

Even without a structured reservoir model, a 4D feasibility study can be conducted with a proven rock physics model and a range of geologic parameters and/or uncertainties in acoustic

parameters such as velocity changes due to stress variations. This study calculates the variation of expected acoustic output based on a range of uncertainty in parameters used as input (porosity, saturation, pore compressibility, and stress-induced velocity coefficients) to a Gulf of Mexico reservoir rock physics model. Input parameters are selected given the three applied depletion methods, i.e., with and without strong aquifer support and water flooding. The results are then applied to a field study.

This thesis consists of three main sections and five appendices. In the Background section, we introduce the Gulf of Mexico reservoir model that is used to simulate depletion methods. We also discuss a few rock physics models and introduce the rock physics and fluid models used in this study. In the Procedure section, we discuss the reservoir depletion modeling methods and the associated variable parameters used per method. The Results section describes the impact of the variable parameters on acoustic properties for each depletion method. In particular, the *Gulf of Mexico Field Example* subsection under Results describes the impact of this study on a particular Gulf of Mexico gas reservoir, which is the overall driver of the study. Finally, the appendices provide additional figures supporting the depletion modeling methods. The four appendices give supplemental plots for specified depletion methods.

Background

Depletion Modeling Methods

We model a particular Gulf of Mexico gas-filled reservoir and simulate three general types of depletion methods. These methods are primary depletion with strong aquifer support, primary depletion with weak aquifer support, and water flood (Batzle et al., 1998). With each depletion method, three or fewer specified parameters like porosity, saturation, and pore compressibility are varied and effects of these parameters on modeled acoustic output are analyzed. Specifically, the effect on bulk density, compressional velocity (Vp), shear velocity (Vs), acoustic impedance, and time thickness is examined in cross plots. The change in amplitude variation with offset (AVO) due to these parameter changes is also examined. We separately define and discuss the parameters to be varied for each depletion method in the Procedures sections.

Pre-Production Reservoir Model Construction

We constructed a pre-production slab model of a Gulf of Mexico gas reservoir (Figure 1). The 175-foot thick reservoir has a 300-foot shale overburden and underburden with identical properties. Reservoir pre-production pore space volume between sand grains, or porosity, is modeled at 30%, and the pore space is filled with 80% gas and 20% water. The net sand per gross thickness, or net-to-gross, in the reservoir layer is 90% as 10% shale is mixed in with the reservoir sands. Modeled parameters are derived from petrophysical evaluations of well logs. For the specified varying parameters, parameter one is varied along the x-axis, parameter two is varied along the y-axis, and parameter three varies with time (Figure 2). The time-variant property is captured in a snapshot of the model at a certain time, which is referred to as a time

step. The three time steps we model over the life cycle of a reservoir are pre-production, depletion, and water flood.

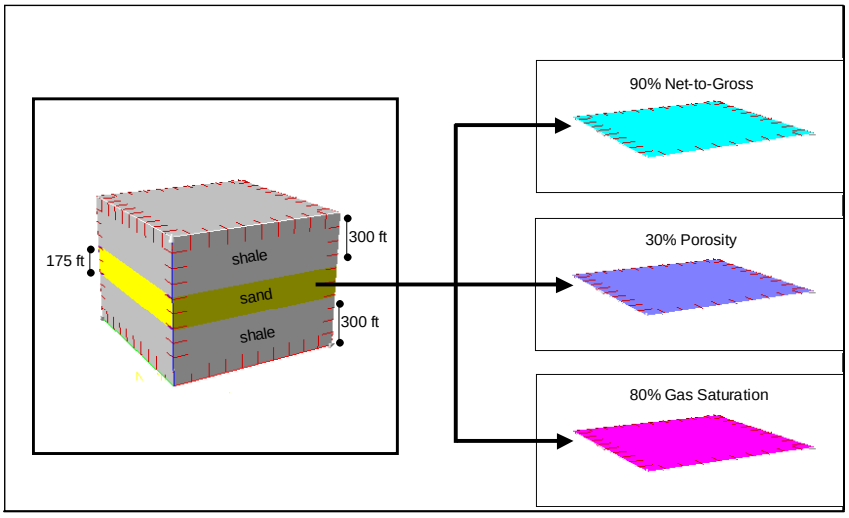

Figure 1: Base reservoir model construction of a particular Gulf of Mexico gas-filled field.

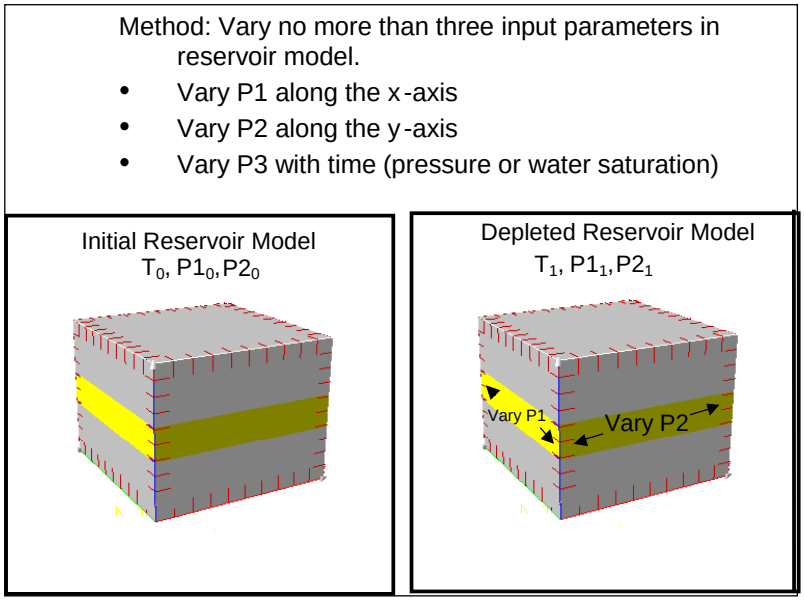

Figure 2: Illustration showing how model parameters will vary over field.

Pore Fluid Model

Pore-filling fluids in the reservoir model are gas-water mixtures. Acoustic properties of the pore-filling fluids are dependant upon reservoir temperature and pressure, along with other constituent properties like, for water, the volume of dissolved salts. Initial reservoir conditions in this model include a pore pressure of approximately 10,000 psi and a temperature of 175 ^{o}F. Resultant modeled water density is approximately 1.02 g/cc and water compressional velocity is 5640 ft/s (bulk modulus is 3.244E7 $ft^2/s^2 g/cm^2$). For gas, density is approximately 0.31 g/cc and compressional velocity is 3001 ft/s (bulk modulus is 2.763E6 $ft^2/s^2 g/cm^2$).

To calculate the density of the fluid mix, we use the Voigt average (Wang, 2001):

$$\rho_f = S_w \rho_w + S_g \rho_g ,$$

where ρ_w and ρ_g are the water and gas densities and S_w and S_g are the water and gas saturation values ($S_w + S_g = 1$). We use Wood's equation (Wang, 2001) to calculate the bulk modulus of the fluid mix, K_f :

$$\frac{1}{K_f} = \frac{S_w}{K_w} + \frac{S_g}{K_g} ,$$

where K_w and K_g are the water and gas bulk moduli, respectively.

Rock Physics Model

Rock physics models quantify the relationship of physical/geological properties of reservoir systems and fluids to elastic properties, such as compressional velocity and shear velocity, which explain seismic signatures (Avseth et al., 2007). Elastic properties from the rock physics model are used in reflection coefficient determination. Numerous rock physics models exist for shaly sands, silty sands, cemented sands, laminated sands, unconsolidated sands, etc. Wang (2001) and Avseth et al. (2007) give nice overviews of various rock physics models that

calculate compressional and shear velocities. We provide a few examples of rock property model equations for sands and shales.

Examples of sand and shale rock physics models

Wet sand, or water-filled, compressional sand velocity typically is calculated as a function of effective stress, porosity, or wet sand density via laboratory experiments. For example, for a clean, wet sand, Han (1986) finds through laboratory experiment that

$$Vp\ (km/s) = 5.59 - 6.93\phi - 2.18C,$$

where ϕ is porosity, and C = 0.05. For a shaley sand, the variable C increases with clay volume.

Some wet sand velocity equations use wet sand density as an argument. Wet sand density is given by

$$\rho_{sand\_wet} = \phi\rho_{water} + (1- \phi\ )\ \rho_{grain,}$$

where ρ_{water} and ρ_{grain} are brine water density and mineral grain density. Typically, these values are 1.0 g/cc to 1.15 g/cc for brine water and 2.65 g/cc for sand (quartz) grains (Avseth et al., 2007).

As an example of a model that relates wet sand compressional velocity to density, consider the Gardner-Gardner-Gregory model (Wang, 2001) given by

$$\rho = 0.23Vp^{0.25},$$

where bulk density ρ has units of g/cm^3 and compressional velocity Vp has units of ft/s. The Gardner-Gardner-Gregory model actually applies to all wet sedimentary rocks, but typically underestimates compressional velocity in wet sands and overestimates compressional velocity in wet shales. This relationship can only be used for wet sediments, and not hydrocarbon-bearing sediments (Wang, 2001).

As an example of a Vp-Vs relationship for wet sands, Castagna et al. (1985) gives the following relationship:

$$Vs(km/s) = 0.8621Vp(km/s) - 1.1724.$$

Han (1986) gives a relationship that is a close fit to Castagna et. al for wet sands, with

$$Vs(km/s) = 0.7936Vp(km/s) - 0.7868.$$

Vp-Vs relationships are critical for fluid identification using amplitude varying with offset (AVO) analysis (Avseth et al., 2007).

Field study rock physics model

For clean, wet sand equations, we used well log data to refine the clean, wet Vp-density and Vp-Vs trends mentioned in the proceeding section. Specifically, wet sand compressional velocity is given by

$$Vp_{wet\_sand}(ft/s) = 21{,}227\rho_{wet\_sand} - 36{,}935,$$

where ρ_{wet_sand} is the wet sand density (g/cc), calculated with a sand grain density of 2.65 g/cc. Also, wet sand shear velocity is given by

$$Vs_{wet\_sand}(ft/s) = 0.894Vp_{wet\_sand} - 3996,$$

where Vp_{wet_sand} is the wet sand compressional velocity (ft/s).

Then, we used fluid substitution techniques (Gassmann, 1951) to introduce hydrocarbon effects to result in pay sand density and compressional and shear velocity products. For each depletion method, appropriate and specified fluid mix properties are used for fluid substitution. We use an additional velocity-stress parameter that accounts for change in velocity due to change in pressure over time due to reservoir depletion. This velocity-stress parameter will be discussed in the primary depletion with weak aquifer support section.

For shale acoustic equations, we use constant Vp, Vs, and density values representative of well log data collected in the bounding shale layers. Specifically, Vp = 9370 ft/s, Vs = 4134 ft/s, and ρ = 2.4 g/cc for the shales. These same shale properties are also used for the 10% shale that is mixed into the modeled reservoir layer.

In our 4D modeling methods, these shale properties are not altered over time for simplification purposes. However, it is noted that the shale layers can experience physical property changes due to reservoir depletion. Particularly, as a reservoir compacts as it is depleted, the surrounding shale layers can experience an expansion. This shale expansion leads to a slight decrease in density and compressional velocity, thus slowing down the travel time of a sound wave traveling through the shale medium (Holt et al., 2005 and Tura et al., 2006) and can decrease the reflection coefficient.

The reservoir layer consists of a mixture of 10% shale and 90% sand, so a mixture of the pay (fluid substituted) sand and shale densities and velocities are used to arrive at bulk properties. The reservoir layer bulk density (ρ_b) is given by the Voigt average (Wang, 2001)

$$\rho_b = f_{sand}\rho_{sand} + (1 - f_{sand})\rho_{shale},$$

where f_{sand} is the net-to-gross (set at 90%), ρ_{sand} is the pay sand density and ρ_{shale} is the shale density. The Reuss (1929) average is used to calculate the reservoir bulk compressional (Vp_b) and shear (Vs_b) velocities:

$$\frac{1}{\rho_b Vp_b^{\,2}} = \frac{f_{sand}}{\rho_{sand} Vp_{sand}^{\,2}} + \frac{1 - f_{sand}}{\rho_{shale} Vp_{shale}^{\,2}}$$

and

$$\frac{1}{\rho_b Vs_b^{\,2}} = \frac{f_{sand}}{\rho_{sand} Vs_{sand}^{\,2}} + \frac{1 - f_{sand}}{\rho_{shale} Vs_{shale}^{\,2}},$$

where Vp_{sand} and Vs_{sand} are the pay (fluid substituted) sand compressional and shear velocities and Vp_{shale} and Vs_{shale} are the shale compressional and shear velocities. On average, the resultant bulk density and bulk compressional velocity nicely fit the respective in situ well log data (Figure 3) in the reservoir sand and bounding shale layers.

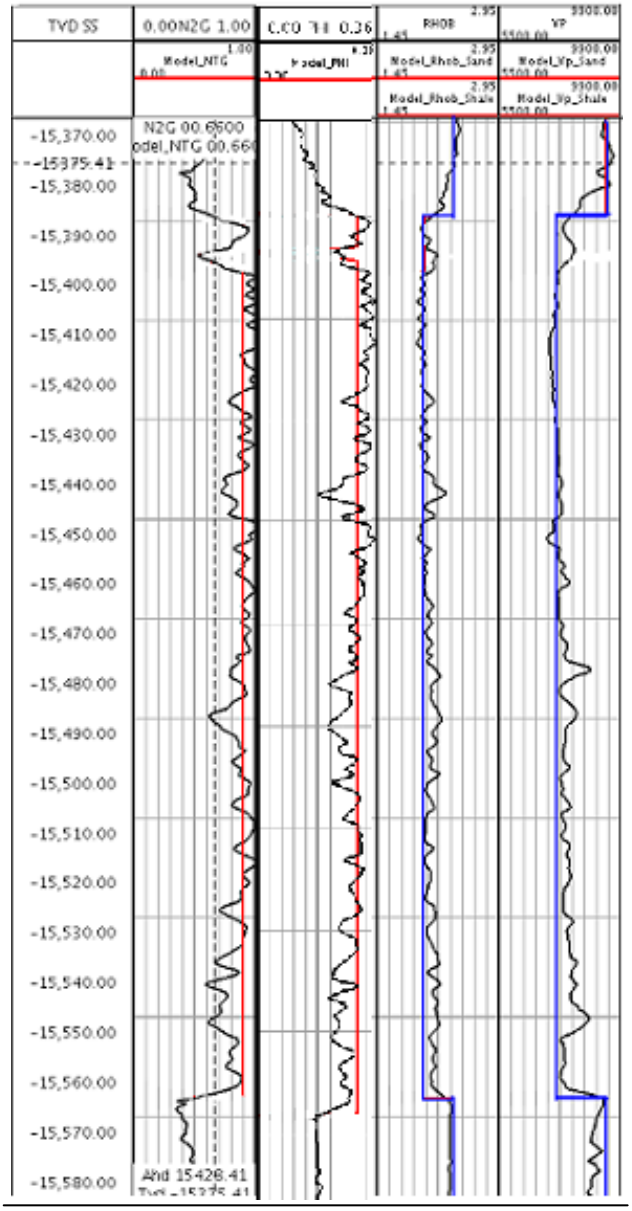

Figure 3: Gulf of Mexico field well net-to-gross, porosity, bulk density, and velocity log data (black, left to right) compared to average reservoir model properties (red) and rock physics model output (blue).

AVO Modeling

AVO effects are modeled using the Shuey (1985) simplification of Aki and Richards 1980 approximation of the complicated Zoeppritz equations (Avseth et al., 2005). Reflection coefficients are calculated for angles of 40 degrees and smaller. Shuey's (1985) approximation for reflection coefficients is given:

$$R(\theta) = R(0) + G\sin^2\theta + F(\tan^2\theta - \sin^2\theta)$$

where

$$R(0) = \frac{1}{2}\left(\frac{\Delta Vp}{\overline{Vp}} + \frac{\Delta\rho}{\overline{\rho}}\right)$$

$$G = \frac{1}{2}\frac{\Delta Vp}{\overline{Vp}} - 2\frac{\overline{Vs}^2}{\overline{Vp}^2}\left(\frac{\Delta\rho}{\overline{\rho}} + 2\frac{\Delta Vs}{\overline{Vs}}\right)$$

and

$$F = \frac{1}{2}\frac{\Delta Vp}{\overline{Vp}}.$$

Here, θ is the angle of incidence in degrees, and $\overline{\rho}$, $\overline{V_p}$, and $\overline{V_s}$ are the average of the densities, compressional velocities, and shear velocities of the interfacing materials.

Procedure

Primary Depletion with Strong Aquifer Support

During depletion with a strong aquifer support, fluids removed from the reservoir are quickly replaced with water from the aquifer. Thus, reservoir pressure remains relatively constant while water saturation increases. We altered the reservoir layer of the pre-production reservoir model to handle a variety of saturation and porosity values. Each cell in this resultant reservoir model represents a possible reservoir saturation case with a specified porosity. For parameter 1, water saturation values vary from 0% to 100%. For parameter 2, porosity values range from 25% to 36%. We calculate bulk density and compressional and shear velocities using the rock property model described in the field study rock physics model section for each saturation and porosity case.

Primary Depletion with Weak Aquifer Support

If a strong aquifer is not present, pore pressure decreases during hydrocarbon production as the fluids removed from pore spaces are not replaced with additional fluids. Since additional water is not coming in from aquifer support, the water and hydrocarbon saturations remain relatively constant. Reduction in pore pressure causes reservoir compaction and decreased reservoir porosity. The amount of reservoir compaction is related to the pore compressibility of the reservoir structure. High pore compressibility results in large reservoir compaction due to a decrease in pore pressure, while low pore compressibility results in a small amount of reservoir compaction due to a decrease in pore pressure. For parameter one, we varied pore compressibilities of the pre-production reservoir model from 25-75 μcips to determine the impact of pore compressibility on acoustic properties. Initial porosity before depletion and compaction is 30%, and fluid saturations remain constant at 20% water and 80% gas.

For parameter two, we varied stress induced velocity changes. The change in wet sand velocity with respect to change in vertical effective stress, $\Delta Vp_{wet}/\Delta\sigma$, or the compressional velocity stress coefficient, is varied from 0 to 0.40. Additionally, $\Delta Vs/\Delta\sigma$ is varied along with, and is equal to, $\Delta Vp_{wet}/\Delta\sigma$. The units of $\Delta Vp_{wet}/\Delta\sigma$ and $\Delta Vs/\Delta\sigma$ are ft/s/psi.

For parameter three, the time variation, we changed the vertical effective stress of the reservoir. Initial vertical effective stress is approximately 2200 psi, and final vertical effective stress is approximately 5000 psi, so the change in vertical effective stress is around +2800 psi. This increase in vertical effective stress, or decrease in pore pressure, causes the reservoir to compact, porosity to decrease, and wet sand velocity to increase. The magnitude of these changes is dependent on the pore compressibility and compressional and shear stress coefficients.

We calculate bulk density and compressional and shear velocities using the rock property model described in the field study rock physics model section for each velocity stress coefficient and pore compressibility case for time steps T_o and T_1, where the change in vertical effective stress is 0 psi and 2800 psi, respectively.

Primary Depletion with Water Flood

In the absence of a strong aquifer, water injection, or water flooding, can be used to increase production rates. During water flood of a reservoir, water is injected into a reservoir via an injection well to push the less dense hydrocarbons towards producing wells and to stabilize/control reservoir pressure. It is not possible to fully characterize the subsurface via seismic data and depositional modeling, thus the injected water does not always flow to the planned targets. Repeat seismic surveys can help monitor water movement due to water injection. Future production decisions are made from these repeat surveys, particularly if water is

not reaching the anticipated target. Water flooding combined with these repeat monitor seismic surveys is very expensive. Between the years 2000 and 2003, companies spent $500 million dollars on 4D seismic services alone (Lumley, 2004). Time-lapse modeling efforts help determine the need and frequency of repeat seismic acquisition.

Over time, water injection will increase reservoir water saturation and pore pressure, possibly resulting in a slight increase in porosity. The increase in porosity is dependent on the initial pore compressibility before compaction (the loading phase), and the pore compressibility after compaction (the unloading phase). We model a reservoir that compacts due to depletion, then slightly re-inflates due to water injection.

Three time steps are included to simulate this depletion method: T_0 represents the undepleted reservoir, T_1 is the compacted reservoir, and T_2 is the water-flooded reservoir. For T_0, we model the undepleted reservoir with water saturation of 20%, porosity of 30%, and varying pore compressibility from 25-75 μcips. For T_1, pore pressure drops by 2800 psi, and water saturation remains at 20% as no fluids are filling depleted pore space. Porosity decreases in this time step depending on the modeled pore compressibility. With the depletion with weak aquifer simulation described in the previous subheading, we varied compressional and shear velocity stress coefficients from 0 to 0.40 ft/s/psi. Here, we restrict the velocity stress coefficient to 0.18 ft/s/psi, thus this T_1 model and its results are a subset of the primary depletion with weak aquifer modeling.

For T_2, the water-flooded reservoir, we increase pore pressure by 500 psi. To simulate the increased water saturations due to water injection, we vary final water saturations from 20% to 100%, corresponding to gas saturations of 80% to 0% respectively. We model high water saturations as we are interested in the acoustic response of a flushed zone to determine if water

movement would be noticeable. Porosity will increase due to pore pressure increase as water moves into pore spaces. The rate of porosity increase is dependent upon the pore compressibility after the T_1 compaction. Soil mechanics experiments have shown that pore compressibility due to unloading is approximately 20% of the initial pore compressibility before loading (Wood, 1990). That is

$$Cp_1 = \frac{1}{5} Cp_0 .$$

We use this 20% assumption to estimate final pore compressibilities in this water flood time step. So, T_0 pore compressibilities vary from 25 to 75 μcips, while after T_1 compaction, pore compressibilites vary from 5 to 15 μcips. This one-to-one correspondence in pore compressibilites results in a one-to-one correspondence between T_1 and T_2 porosity values. To determine this relationship in terms of Cp_0, first consider T_2 porosity values can be calculated by

$$\phi_2 = \phi_1 (1 - Cp_1 \Delta\sigma) .$$

With $\Delta\sigma$ = -500 psi and substituting in the equation above, we have

$$\phi_2 = \phi_1 (1 + 100 Cp_0) .$$

Also,

$$\frac{\phi_2 - \phi_1}{\phi_1} = 100 Cp_0 ,$$

so the percent change of porosity between compaction and water injection phases is $10{,}000Cp_0$ or $50{,}000Cp_1$. For the highest initial pore compressibility of Cp_0 = 75 μcips, the percent change in porosity between compaction and water injection phases is 0.75%.

We calculate bulk density and compressional and shear velocities using the rock property model described in the field study rock physics model section for each saturation and porosity case for time steps T_o, T_1, and T_2 with changes in vertical effective stress of 0 psi, -2800 psi, and +500 psi, respectively.

Model Results

Primary Depletion with Strong Aquifer Support

For reference, Table 1 lists the ranges of the varied parameters used for modeling this depletion method. For further details on these parameters, refer to the PROCEDURES section for this depletion method.

Time	**X**	**Y**
0	$25\% \leq \Phi \leq 36\%$	$0 \leq S_w \leq 100\%$

Table 1: Ranges of varied parameters in depletion with strong aquifer support modeling.

Figure 4 shows how bulk density, compressional velocity, shear velocity, and bulk modulus change with various water saturations for certain porosity values. Water saturation values in this plot and all following plots are shown in decimal equivalents to the percentages. Each contour line represents a different porosity value. As water saturation increases, bulk density increases linearly (Figure 4a). This increasing behavior is expected as the density of water is higher than the density of gas. Lower porosity values result in higher bulk density, as sand grain density values are higher than the pore space-filling fluids. The behavior of compressional velocity with respect to water saturation is nearly linear until water saturation becomes higher than 70% (Figure 4b). The cross plot of water saturation versus shear velocity has near zero slope for each porosity case (Figure 4c) because water saturation has little effect on shear velocity as fluids do not shear. The slight decrease in shear velocity with respect to increase in water saturation is due to the changing bulk density. Low porosity values result in higher shear velocity effects as the structure matrix components are subject to shear (Figure 4c). As the water saturation increases, the fluid mix becomes less compressible, thus the bulk modulus increases (Figure 4d). As with compressional velocity, adding a small amount of gas makes a large impact on bulk modulus since gas is highly compressible.

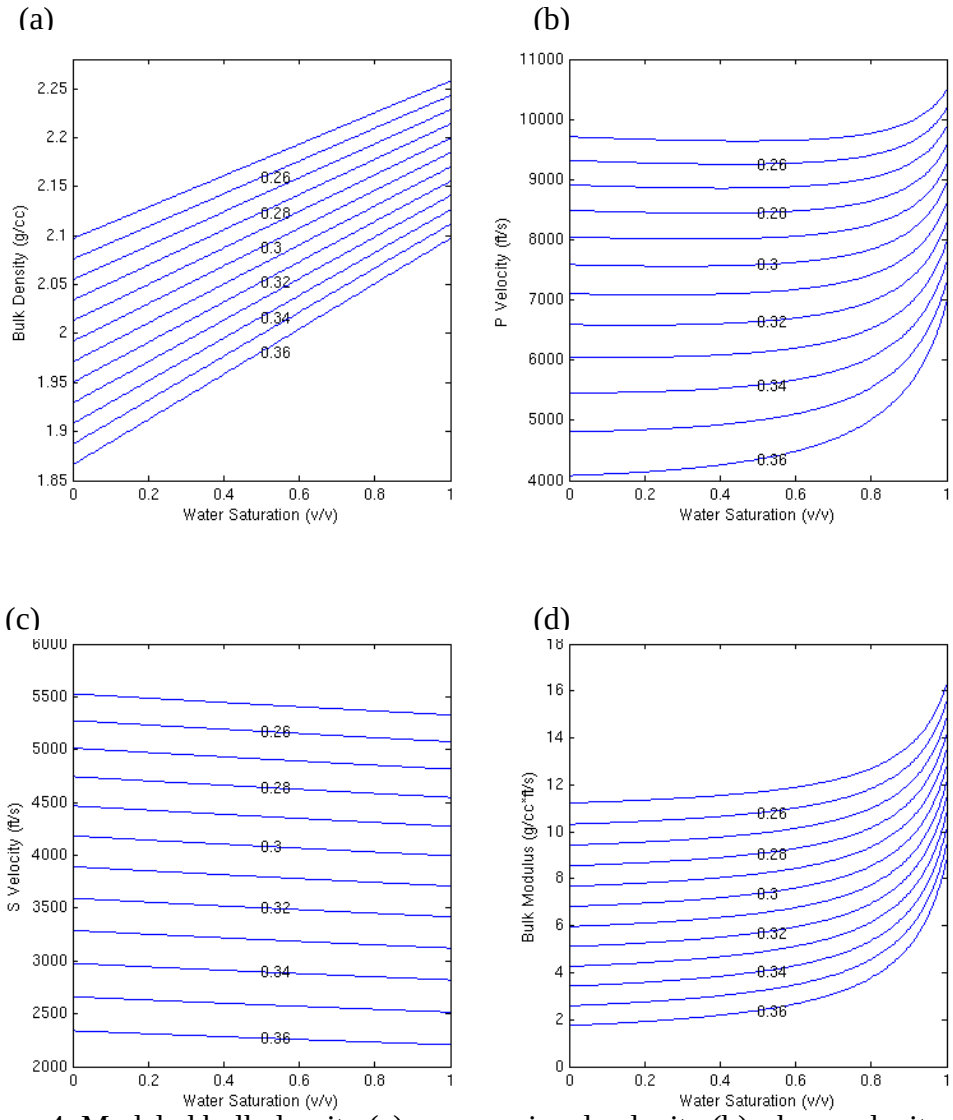

Figure 4: Modeled bulk density (a), compresional velocity (b), shear velocity (c), and bulk modulus (d) as fluid changes from 0% water to 100% water, or 100% gas to 0% gas. Water saturation values in plots are shown in decimal equivalents. Contour lines represent porosity cases of 25% to 36%.

Figure 5 shows how acoustic impedance, which is the product of bulk density and compressional velocity, and time thickness change with water saturation for certain porosity values. Increasing water saturation increases compressional velocity and density, thus increasing acoustic impedance (Figure 5a). As water compressional velocity is larger than gas, increasing water saturation speeds up velocity, so wave travel time through the fluid decreases (Figure 5b).

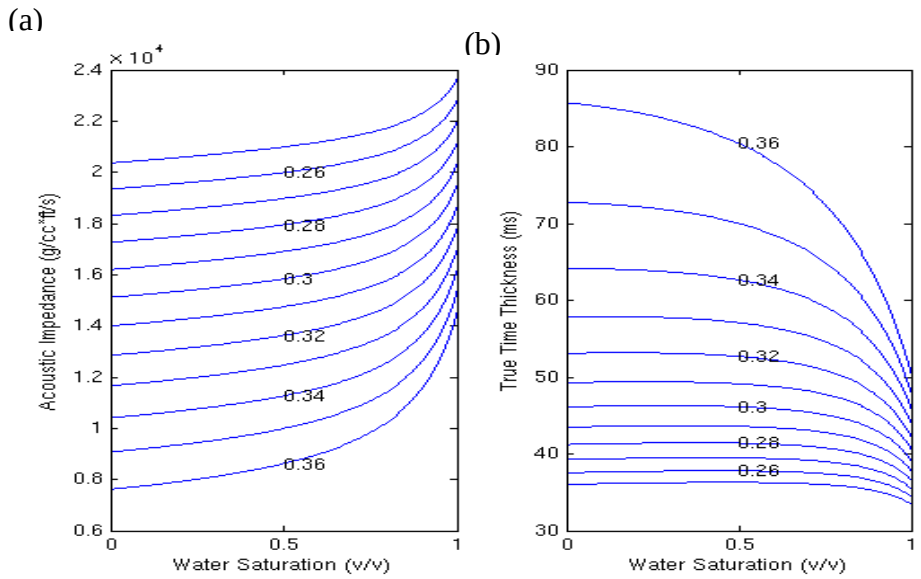

Figure 5: Modeled acoustic impedance and time thickness as fluid changes from 0% water to 100% water, or 100% gas to 0% gas. Contour lines represent porosity cases of 25% to 36%.

Figure 6 illustrates the AVO behavior with varying water saturations, with angles 0 to 40 degrees on the x-axis, and reflection coefficient (RFC) on the y-axis. We present three different porosity cases: 26%, 30%, and 34%. Each contour represents a different water saturation, which is labeled. For the low 26% porosity case, we see a typical gas sand Class III AVO behavior with a negative intercept and gradient when water saturation is 80% or below. Class II AVO behavior is exhibited in the 100% water case. Here, we have a negative gradient with increasing angle. Since this 100% water case starts with a positive intercept and has a polarity change (here around 15 degrees), this can further be refined as a Class IIp anomaly as designated by Ross and Kinman (Per Avseth et al., 2005).

For the mid 30% porosity case, we again see typical Class III AVO behavior for a gas filled sand when water saturation is 80% or below. For the 100% water case, Class IV AVO behavior is observed. Class IV AVO anomalies are not often observed. Here we have a negative intercept but positive gradient.

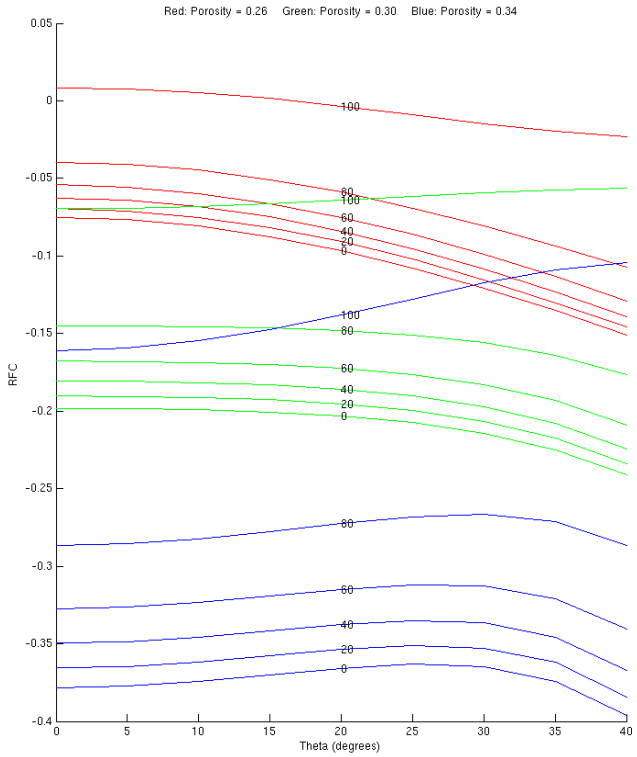

Figure 6: AVO behavior of the reflection coefficients for water saturations (labeled contours) ranging from zero to 100%. Three porosity cases are represented with 26% porosity in red, 30% porosity in green, and 34% porosity in blue.

As for the high 34% porosity case, we again see the rare Class IV AVO behavior for the 100% water case. However, the AVO behavior for the 80% and below water cases has an unusual shape. In the near to mid angle ranges (angles 0 to 25 degrees), Class IV AVO behavior is exhibited. In the mid to far angle ranges (angles 25 to 40 degrees) a negative gradient consistent with Class II behavior begins. This behavior is seen with the higher porosity values of 31% to 36%. For a more detailed look at AVO behavior for additional porosity values, Appendix A presents cross plots of water saturation versus reflection coefficient and porosity versus reflection coeffcient for angles 0, 10, 20, 30, and 40 degrees. Appendix B presents cross plots showing change in reflection coefficient and percent difference in reflection coefficient for various cases.

To further examine change in AVO behavior and to determine if there are advantages to studying near angle AVO behavior versus far angle AVO behavior, we consider the case when water saturation increases from 20 percent to 60 percent for porosities 26, 30, and 34 percent. Increasing water saturation decreases the magnitude of the reflection coefficient, but the shape of the curve remains nearly unchanged as shown in Figure 6. At every angle, the change in reflection coefficient is calculated for each porosity case (Figure 7). The change in reflection coefficient is much larger at the higher 34% porosity case than the other porosity cases. In the 34% porosity case, the larger angle of incidence ranges will show a larger change in reflection coefficient than the smaller angle of incidence ranges. This is also holds for the 26% and 30% porosity cases, however, the differences are not as dramatic. When water saturation increases, the largest change in magnitude of reflection coefficient occurs in the large angle ranges, although this may not be considerably larger than the change in the smaller angle ranges for smaller porosity cases.

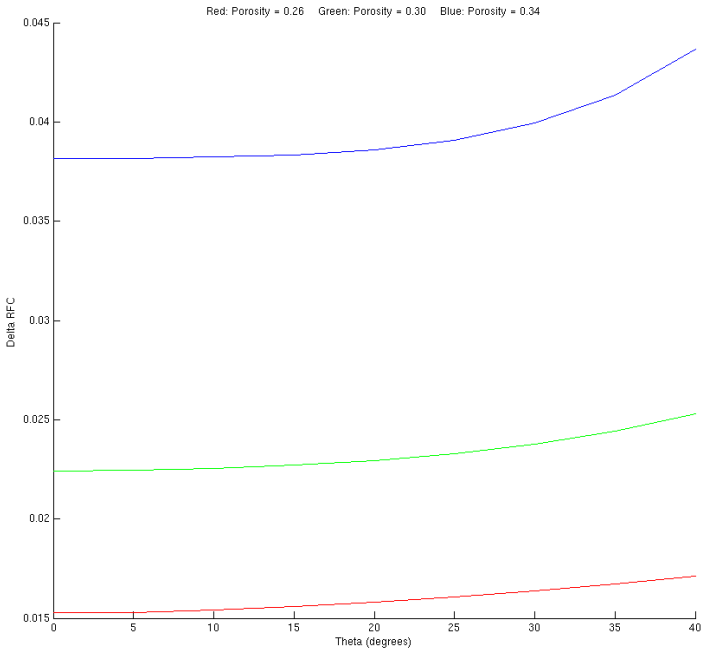

Figure 7: Change in reflection coefficient for angles of incidence ranging from 0 to 40 degrees due to a change in water saturation from 20% to 60%. Three porosity cases of 26%, 30%, and 34% are shown in red, green, and blue, respectively.

The percent difference ($\Delta RFC/RFC_2$) in reflection coefficient exhibits much more interesting behavior (Figure 8). The 34% porosity case (blue) suggests the largest percent difference can be seen in the large angle range an almost 12% decrease in reflection coefficient. However, the small angle range decrease is greater than 10%. Opposite to this is the percent difference in reflection coefficient for the 30% porosity case (green) as the percent difference is near 12% in the small angle range and approaches 10% in the large angle range. For the low 26% porosity case (red), a 22% change in reflection coefficient occurs at the small angle range and a greater than 12% change in reflection coefficient occurs at the middle angle range. Thus, at small porosity, the greatest percent difference in reflection coefficient can be seen at the small angle ranges. The behavior of the low 26% porosity case is due to the small magnitude of the reflection coefficients in the denominator of the percent difference calculation.

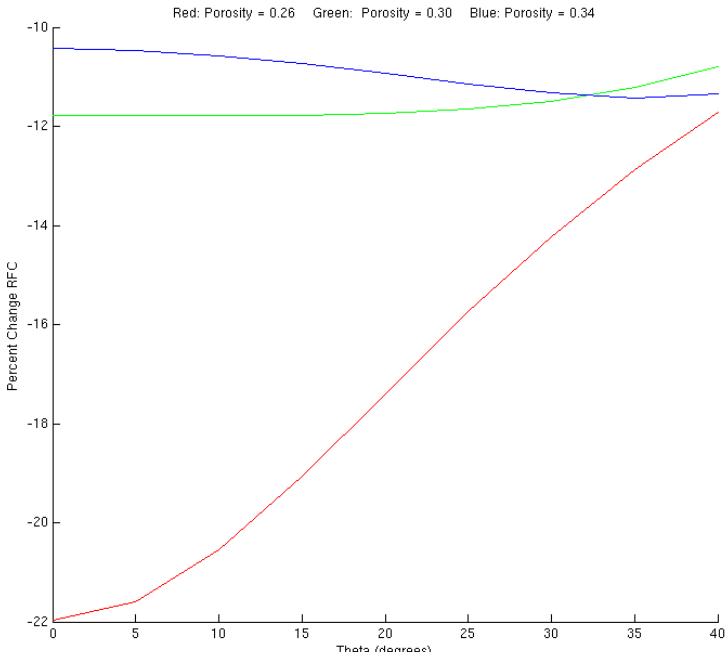

Figure 8: Percent difference in reflection coefficient for angles of incidence ranging from 0 to 40 degrees due to a change in water saturation from 20% to 60%. Three porosity cases of 26%, 30%, and 34% are shown in red, green, and blue respectively.

In summary, when considering the absolute change in reflection coefficients, the largest change will be seen at large angles of incidence. When considering the percent difference in reflection coefficient, the largest percent difference is seen at large angles of incidence for a high porosity of 34%, but at small angles of incidence for lower porosities. Also, if a large percent difference in reflection coefficients occurs at the near angle range, but not at the far angle range, a low porosity zone can be expected as seen by comparing the 26% porosity case to the other porosity cases.

Primary Depletion With Weak Aquifer Support

For reference, Table 2 lists the ranges of the varied parameters used for modeling this depletion method. For further details on these parameters, refer to the PROCEDURES section for this depletion method.

Time	**X (unit *μcips*)**	**Y (unit *ft/s/psi*)**	**ΔVES**
0 (undepleted)	$25 \leq Cp_0 \leq 75$	$0 \leq \Delta Vp_{wet}/\Delta\sigma \leq 0.40$	0 psi
1 (depleted)	$Cp_1 = 0.2Cp_0$	$0 \leq \Delta Vp_{wet}/\Delta\sigma \leq 0.40$	+2800 psi

Table 2: Ranges of varied parameters in depletion with weak aquifer support modeling. Time 0 porosity is 30%, and Time 0 and Time 1 water saturation is 20%.

We calculate bulk density and compressional and shear velocities using the rock property model previously described for each time step. For the undepleted reservoir at the initial time step, T_0, resultant bulk density and velocities will be constant across the slab model as porosity and water saturation is constant. For the depleted reservoir at the final time step, T_1, resultant bulk density and velocities will not be constant as the pore pressure has been reduced causing porosity decrease and sand velocity increase.

Figure 9 shows how porosity, bulk density, and compressional and shear velocities change after compression. Figure 9a plots the pore compressibility versus the final porosity due to the decrease in pore pressure. Final porosity (ϕ_f) is calculated from initial porosity (ϕ_i), pore

compressibility (Cp), and change in effective stress ($\Delta\sigma$), and is given by the following relationship: $\phi_f = \phi_i (1\text{-}Cp\Delta\sigma)$.

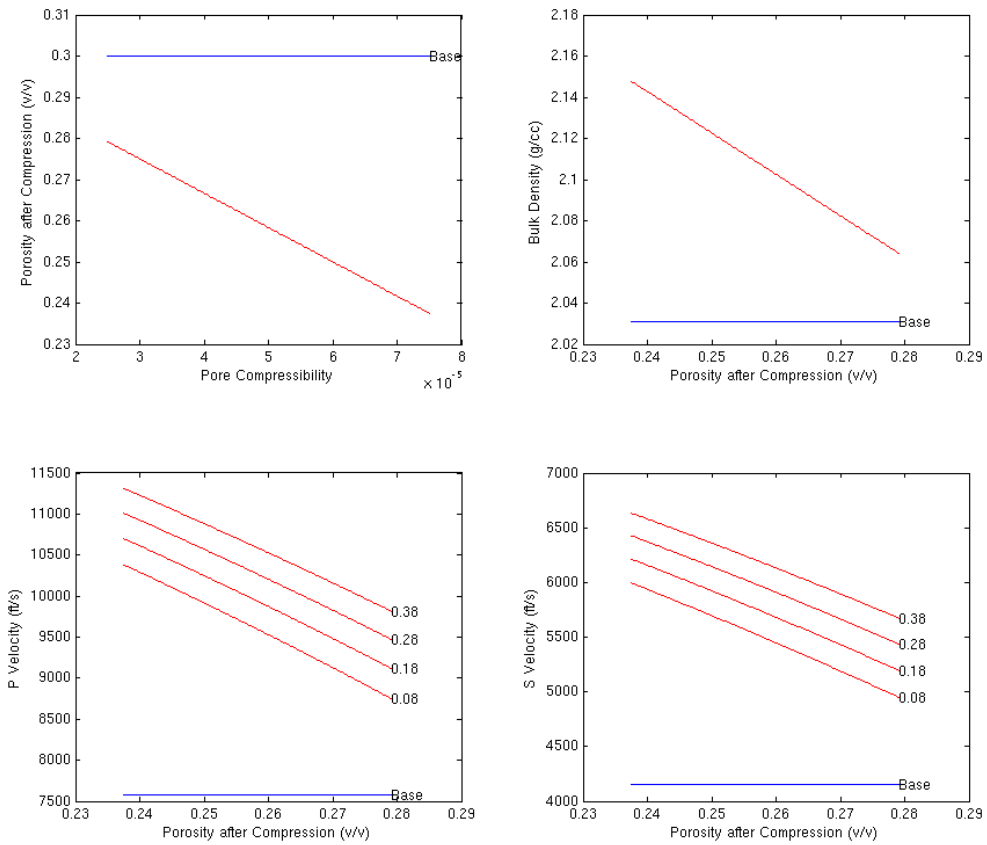

Figure 9: (a) Modeled final porosity as pore compressibility varies from 25 μcips to 75 μcips in red. Modeled final (b) bulk density, (c) compressional velocity, (d) and shear velocity as final porosity after compression varies from approximately 23% to 28%. Labeled contours give values for the different cases of velocity stress coefficients where applicable. Initial (base) case shown as reference in blue.

As previously stated, the initial porosity is 30%, and the change in stress from the initial time step to the final time step is approximately 2800 psi. Thus, pore compressibility is the only varying factor that influences final porosity. For the highest pore compressibility of 75 μcips, porosity drops from 30% to 24%. For the lowest pore compressibility of 25 μcips, porosity drops from 30% to 28%. As there is a one-to-one relationship between initial and final porosity values,

all remaining cross plots in this section will list final porosity after compaction on the x-axis instead of pore compressibility.

T_0 bulk density is approximately 2.03 g/cc. The T_1 bulk density is dependent upon the final porosity, which varies with compressibility as discussed in the previous paragraph. Higher final T_1 porosity values lead to lower bulk density values (Figure 9b). The results shown for bulk density are a subset of the results of the previous section with a water saturation of 20%. The largest change in bulk density from the initial case bulk density of approximately 2.03 g/cc occurs at the minimum final porosity value of 23.8% (Figure 9a), where final bulk density is approximately 2.15 g/cc.

T_0 compressional velocity is approximately 7,580 ft/s. The T_1 bulk velocity is dependent upon final bulk density and the velocity stress coefficient. As we are varying the velocity stress coefficients, multiple cases are considered. Larger stress coefficients lead to larger final bulk velocity (Figure 9c). With the modeled change in stress, adding 0.1 ft/s/psi to the stress coefficient results in increasing bulk velocity by approximately 300 ft/s. Similar effects are seen in shear velocity, where the initial shear velocity is approximately 4,150 ft/s (Figure 9d).

T_0 acoustic impedance is approximately 15400 g/ccft/s. The T_1 acoustic impedance is dependent upon final bulk density and compressional velocity. T_1 acoustic impedance increases as final porosity and stress coefficients increase (Figure 10a), and varies from 1.8×10^4 to 2.5×10^4 g/cc ft/s.

T_0 reservoir time thickness (Figure 10b) is approximately 46 ms. T_1 time thickness is dependent upon final compressional velocity, and varies from 28 ms to 39 ms as shown in Figure 10b. As the compressional velocity is increasing, the final time thickness decreases. Final T_1

time thickness is the smallest for the lowest final porosity and highest velocity stress coefficient. In this case, time thickness drops from 46 ms to 28 ms.

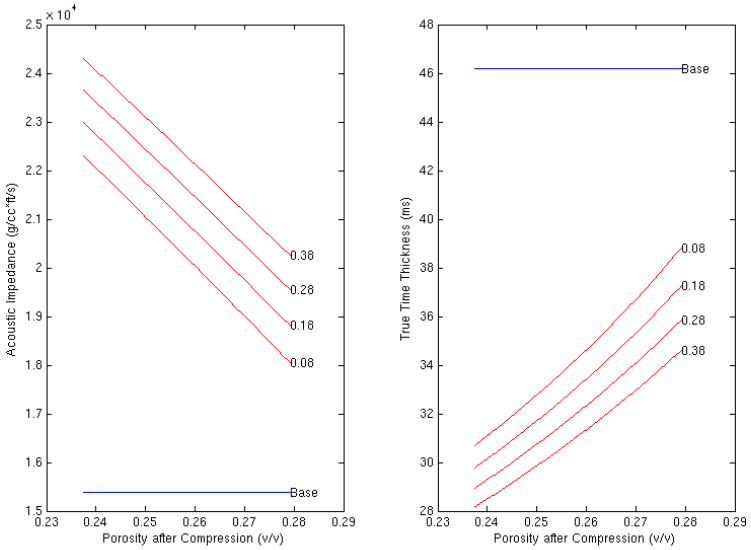

Figure 10: Modeled final acoustic impedance (a) and time thickness (b) as final porosity after compression varies from approximately 23% to 28%. Labeled contours give values for the different cases of velocity stress coefficients. Initial (base) case shown as reference in blue.

T_0 case AVO behavior is Class III with a negative intercept and gradient, which is typical of a gas-filled sand. As pressure in the reservoir drops during depletion, we can expect changes in the AVO behavior. Regardless of the velocity stress coefficient used in this study, a negative gradient exists in the angle versus reflection coefficient plots after modeled depletion. Figure 11 illustrates this for the velocity stress coefficient of 0.18 ft/s/psi. Examples for other velocity stress coefficients are included in Appendix C. For smaller porosities, which are resultant from higher pore compressibilities, we see a change in polarity when stress coefficients are 0.18 and higher. This is again the rare Class IIp behavior with a negative gradient but positive intercept. A change from the base case Class III to the Class IIp AVO behavior can be expected after depletion and compaction when the reservoir comprises highly compressible sands and the expected change in wet sand velocity due to stress change is high (greater than 0.18 ft/s/psi).

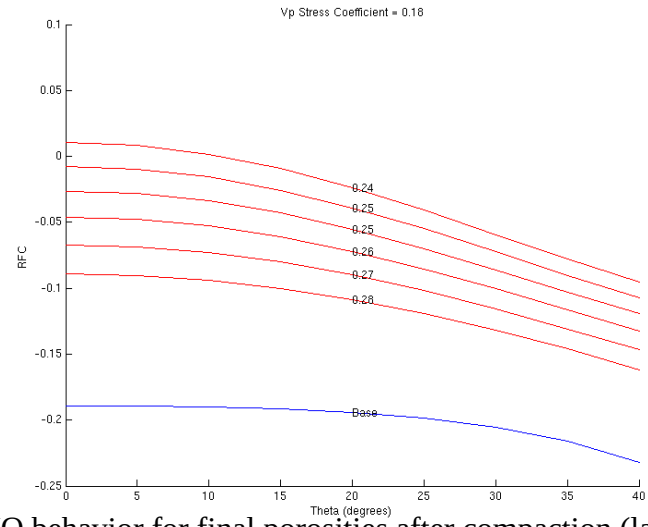

Figure 11: AVO behavior for final porosities after compaction (labeled contours) ranging from 24% to 28% when velocity stress coefficient of 0.18. Initial (base) case with porosity of 30% is shown as reference in blue.

The largest change in reflection coefficient will be seen at small angles of incidence when comparing the initial reflection coefficient to the final reflection coefficient (Figures 12, 13, 14). Figure 12 shows the reflection coefficient, Figure 13 shows the change in reflection coefficient, and the fractional difference in reflection coefficient is given in Figure 14. As the angle of incidence increases, the change in reflection coefficient decreases. Less compressible sands (higher final porosities) result in a lower change in reflection coefficient. Looking at percentages, the highest compressible sands (75 μcips) paired with the largest modeled velocity stress coefficients will result in over a 120% reduction in reflection coefficient at normal incidence, and 65% reduction in reflection coefficient at a 40-degree angle of incidence. The smallest modeled percent reduction in reflection coefficient is at just over 20%. This smallest percent reduction is seen at a 40-degree angle of incidence for the least compressible sands and lowest velocity stress coefficient.

In summary, the smallest change in reflection coefficient at normal incidence is a reduction of 40% while the largest at normal incidence is a reduction of 120%, depending on compressibility and velocity stress coefficients. The smallest percent reduction at a 40-degree angle of incidence is around 25% while the largest at a 40-degree angle of incidence is around 65%, depending on compressibility and velocity stress coefficients.

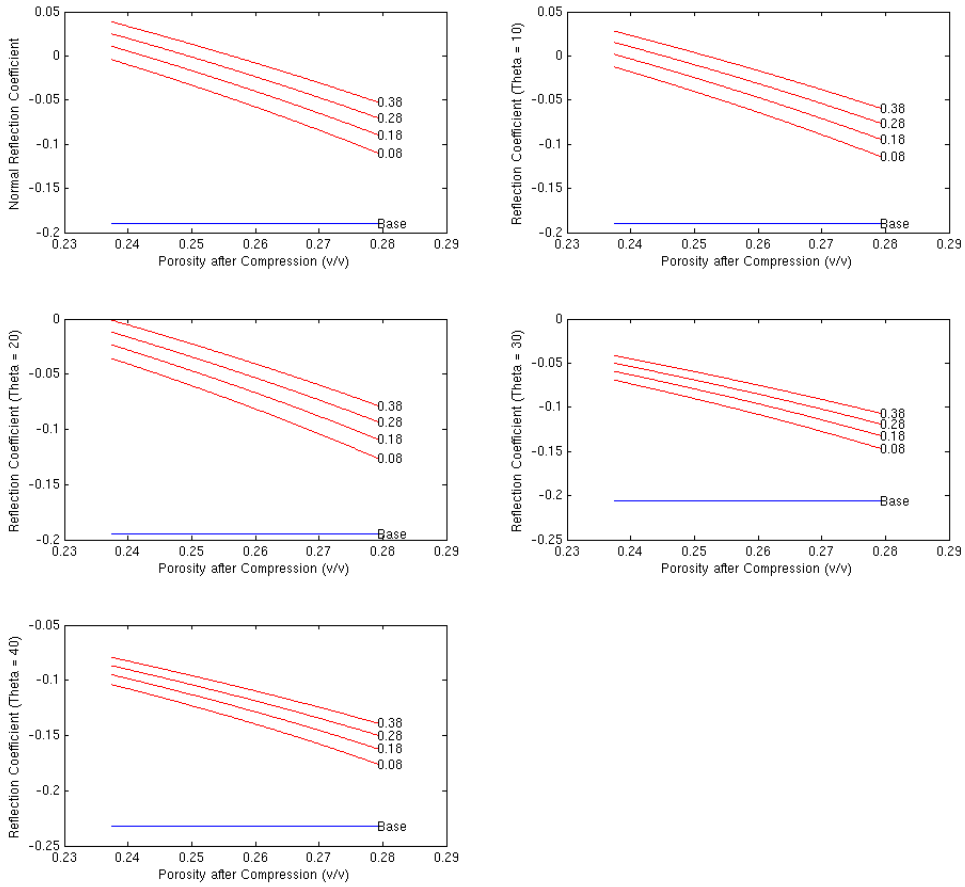

Figure 12: Reflection coefficient for angle of incidence 0 (a), 10 (b), 20 (c), 30 (d), and 40 (e) degrees versus final porosity after compaction. Labeled contours show various velocity stress coefficients. Base case reflection coefficient is shown for reference for each angle in blue.

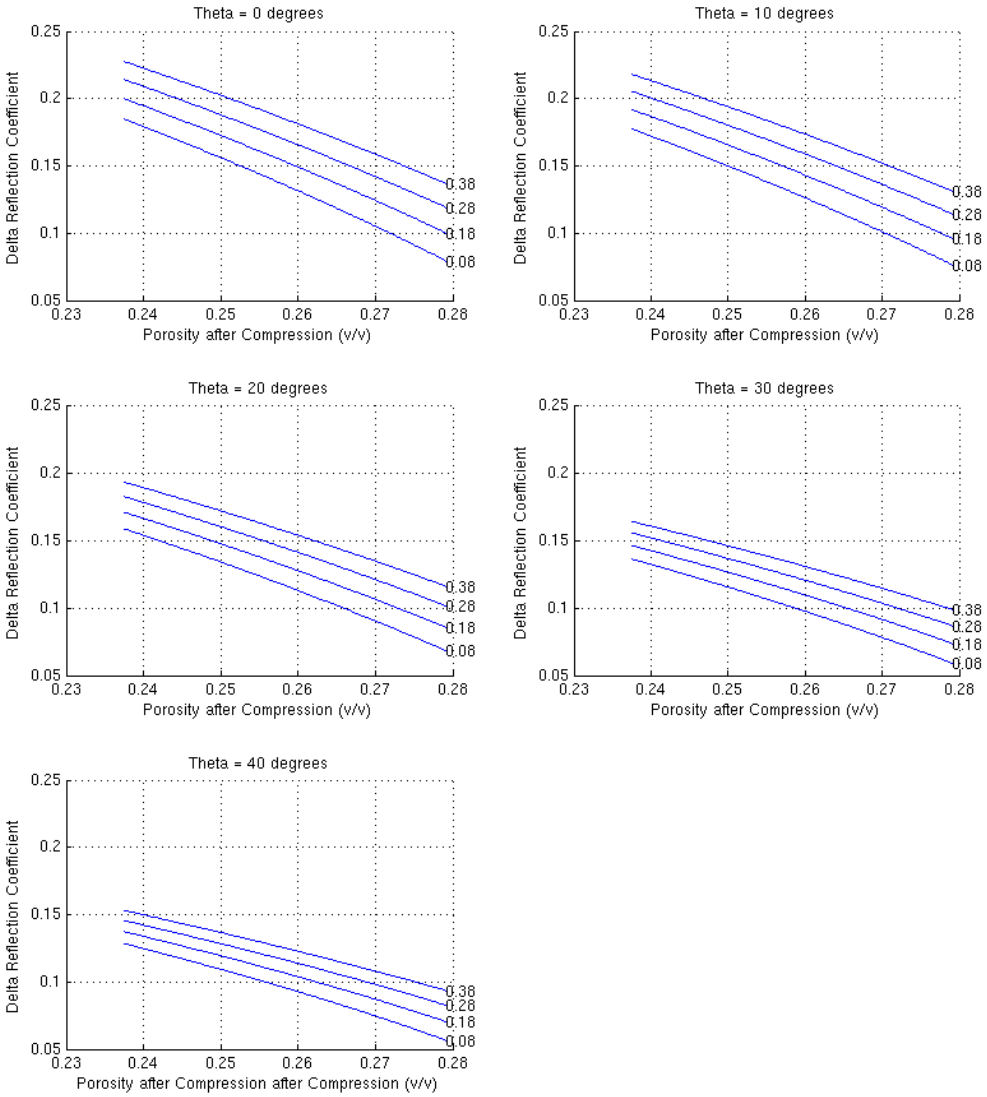

Figure 13: Change in reflection coefficient for angle of incidence 0 (a), 10 (b), 20 (c), 30 (d), and 40 (e) degrees versus final porosity after compaction. Labeled contours show various velocity stress coefficients.

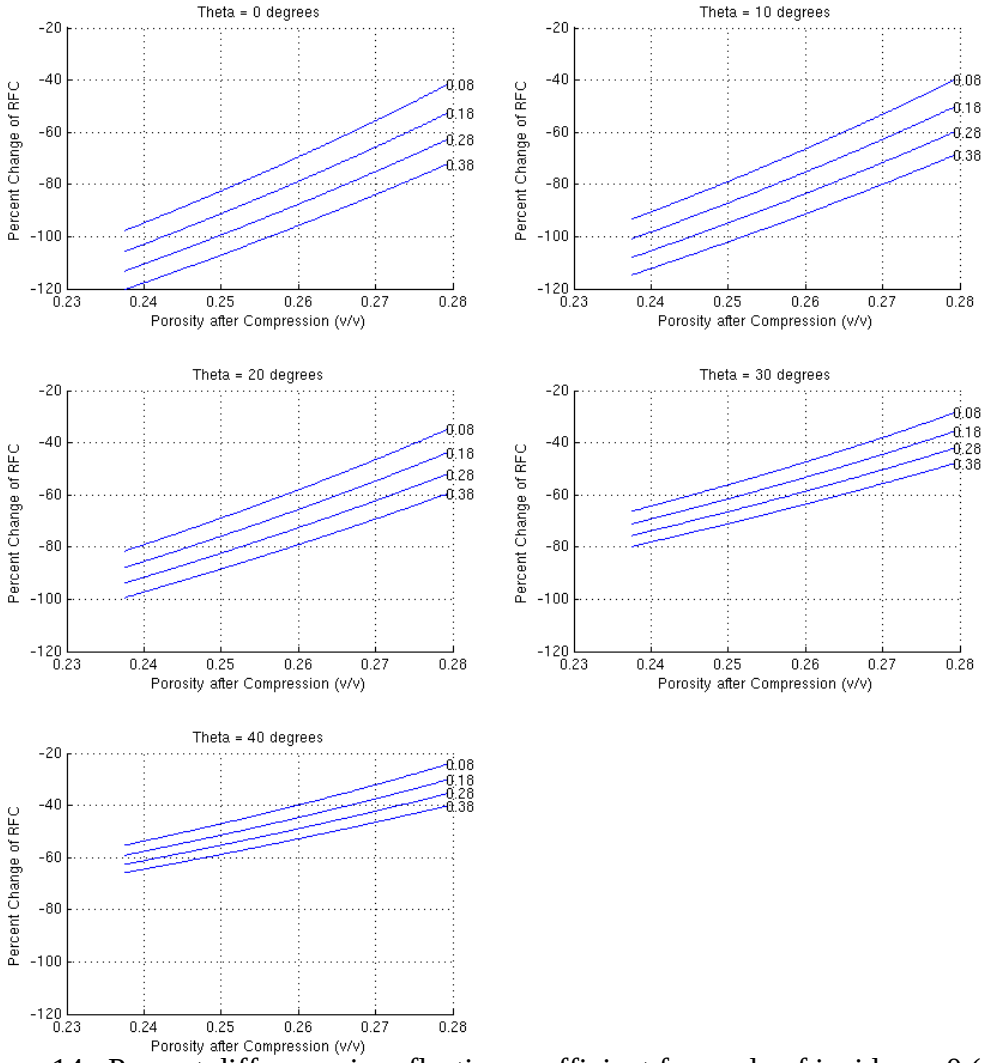

Figure 14: Percent difference in reflection coefficient for angle of incidence 0 (a), 10 (b), 20 (c), 30 (d), and 40 (e) degrees versus final porosity after compaction. Labeled contours show various velocity stress coefficients.

Primary Depletion With Water Flood

For reference, Table 3 lists the ranges of the varied parameters used for modeling this depletion method. For further details on these parameters, refer to the PROCEDURES section for this depletion method.

Time	**X (unit *μcips*)**	**Y**	**ΔVES**
0 (undepleted)	$25 \leq Cp_0 \leq 75$	$S_w = 20\%$	0 psi
1 (depleted)	$Cp_1 = 0.2Cp_0$	$S_w = 20\%$	+2800 psi
2 (water flooded)	$Cp_2 = 1.05Cp_1$	$20 < S_w \leq 100\%$	-500 psi

Table 3: Ranges of varied parameters in depletion with water flooding modeling. Time 0 porosity is 30%, and Time 0 and Time 1 water saturation is 20%. The velocity stress coefficients are 0.18 ft/s/psi for all times.

Figure 15 relates porosity to time steps for each pore compressibility. Figure 16a illustrates how density changes for T_0 and T_1 with respect to T_1 porosity for various final water saturations. The x-axis on this plot and subsequent plots in this section is T_1 porosity. It is useful to plot the x-axis with T_1 porosity instead of T_2 porosity as a vertical line can be drawn from the depletion case to resulting water flood cases without having to separately calculate T_2 porosity. T_0 reservoir density is a constant 2.03 g/cc. As the pressure drops and the reservoir compacts, porosity decreases and T_1 density increases to values between 2.06 g/cc and 2.15 g/cc, depending on pore compressibility. As the reservoir inflates due to water injection, T_2 density increases to values between 2.13 g/cc and 2.27 g/cc, depending on final water saturation. The slight increase in porosity due to pressure increase in T_2 does not cause a density reduction as an increase in water saturation accompanies this increase in porosity.

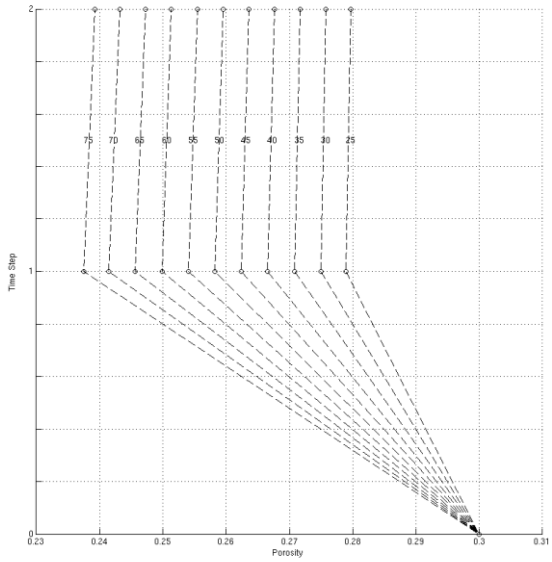

Fig 15: Porosity values (x axis) for each modeled time step (y axis) where y value 0 is the constant T_0 initial model, 1 is the T_1 depleted model, and 2 is the T_2 water-flooded model for labeled pore compressibilies ranging from 25- 75 μcips. Pressure decreases by 2800 psi between T_0 and T_1, and increases by 500 psi between T_1 and T_2.

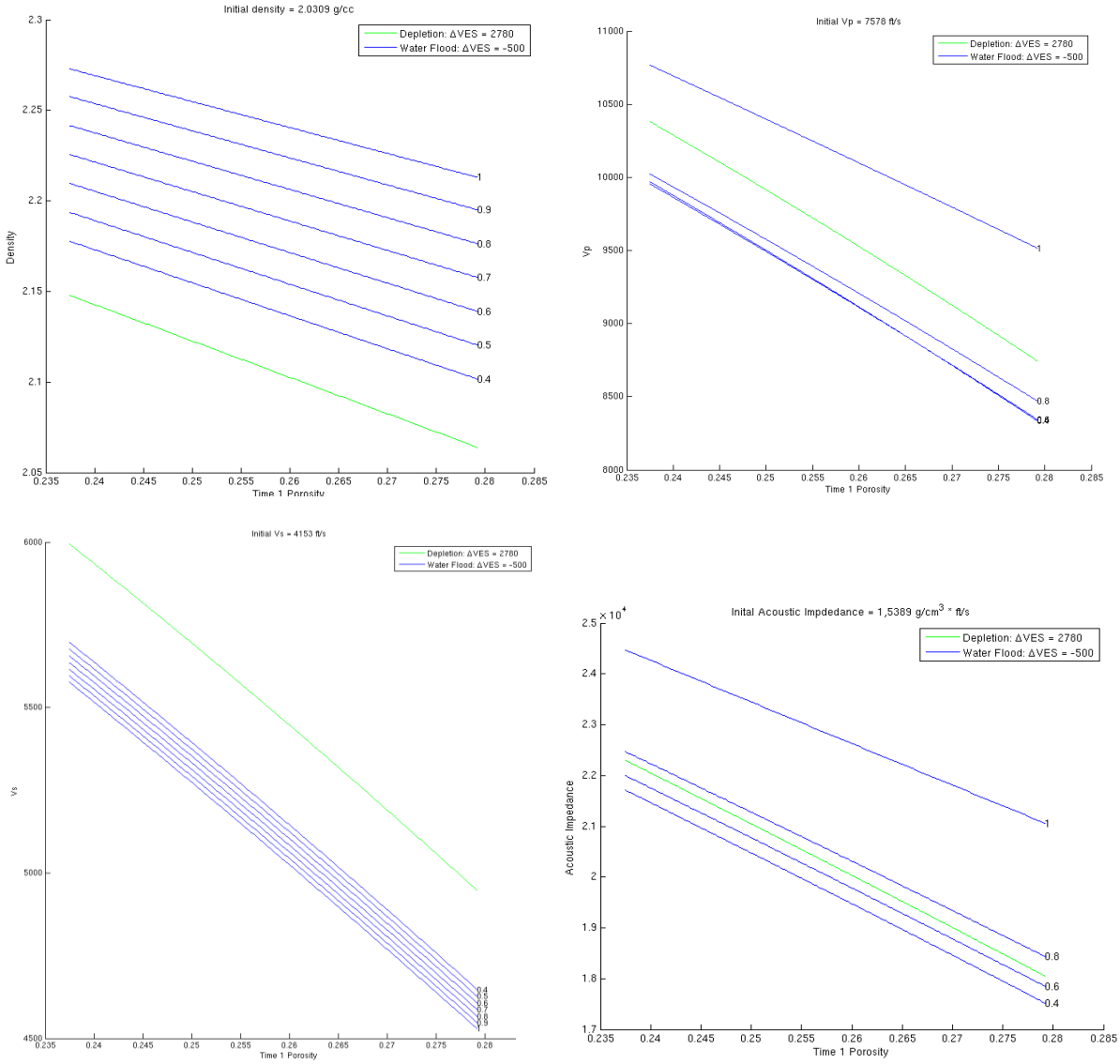

Fig 16: Density (a), compressional velocity (b), shear velocity (c) and acoustic impedence (d) versus depleted time 1 porosity. Time 1 depleted values shown in green. Time 2 water flooded values shown in blue for various labeled final water saturations. Time 0 values are shown in the title of each plot. Units for y-axis values are the same as time 0 value units shown in the title.

Figure 16b illustrates how compressional velocity changes for T_0 and T_1 with respect to T_1 porosity. T_0 compressional velocity is a constant 7578 ft/s. As pressure drops and the reservoir compacts, T_1 compressional velocity increases to values between 8,700 ft/s and 10,400 ft/s, corresponding to T_1 end member porosities after compression of 28% and 24% respectively. After inflation and water flood, compressional velocity actually decreases even though water compressional velocity is higher than gas compressional velocity. Resulting compressional velocity for water saturation cases of 40-60% are virtually indistinguishable. Only with T_2 water saturation greater than 95% does T_2 compressional velocity exceed T_1 compressional velocity.

Figure 16c illustrates how shear velocity changes for T_0 and T_1 with respect to T_1 porosity. T_0 shear velocity is a constant 4,153 ft/s. As pressure drops and the reservoir compacts, T_1 shear velocity increases to values between 4,950 ft/s and 5,990 ft/s, corresponding to T_1 end member porosities after compression of 28% and 24%, respectively. After inflation and water flood, shear velocity decreases to values between 4,500 ft/s and 5,400 ft/s, depending on T_2 porosity and water saturation. As fluids do not shear, shear velocity is not very sensitive to fluid change. For each T_1 porosity case, the shear velocity decreases by approximately 125 ft/s as water saturation is increased from 40% to 100%. This change in shear velocity is caused by the increase in bulk density as water saturation increases. Even with the highest water saturation case, T_2 shear velocity never drops back down to the initial T_0 shear velocity.

Figure 16d illustrates how acoustic impedance changes for T_0 and T_1 with respect to T_1 porosity. T_0 acoustic impedance is a constant 15,380 (ft/s)(g/cm^3). As pressure drops and the reservoir compacts, T_1 acoustic impedance increases to values between 18,050 (ft/s)(g/cm^3) and 22,295 (ft/s)(g/cm^3), corresponding to T_1 end member porosities after compression of 28% and

24%, respectively. After T_2 inflation and water flood, acoustic impedance decreases to values between (17,500 ft/s)(g/cm^3) and 22,000 (ft/s)(g/cm^3) if the final water saturation is 60% and lower, depending on T_2 porosity and water saturation. For high water saturations of 80% and higher, acoustic impedance actually increases between T_1 and T_2.

Figure 17 illustrates the change in time thickness between T_0 and T_1, and T_0 and T_2 with respect to T_1 porosity. T_o initial time thickness is a constant 46 milliseconds. As pressure drops and the reservoir compacts, the decrease in time thickness between T_0 and T_1 ranges from 8 milliseconds to 15 milliseconds, corresponding to T_1 end member porosities after compression of 28% and 24%, respectively. After T_2 inflation and water flood, the time thickness decreases even further and is smaller for larger water saturations. This decrease in time thickness between T_2 and T_0 ranges from 5 milliseconds to 14 milliseconds, corresponding to T_1 end member porosities after compression of 28% and 24%, respectively, when the T_2 final water saturation is 60% or less. When T_2 final water saturation is 70% or less, the change in time thickness is nearly identical for all compressibility cases. This means that T_2 time thickness for the 25% water saturation case cannot easily be distinguished from the 70% water saturation case, regardless of compressibility/final porosity. The final water saturation cases become distinguishable by approximately 1 millisecond only for very high water saturations. For instance, the 80% T_2 water saturation case and the 60% T_2 water saturation case differ by 1 millisecond when paired with the highest T_1 porosity/lowest pore compressibility. Thus, when water flooding a gas reservoir, it can be very difficult to differentiate between final water saturation cases that are less than 70% by examining change in time thickness.

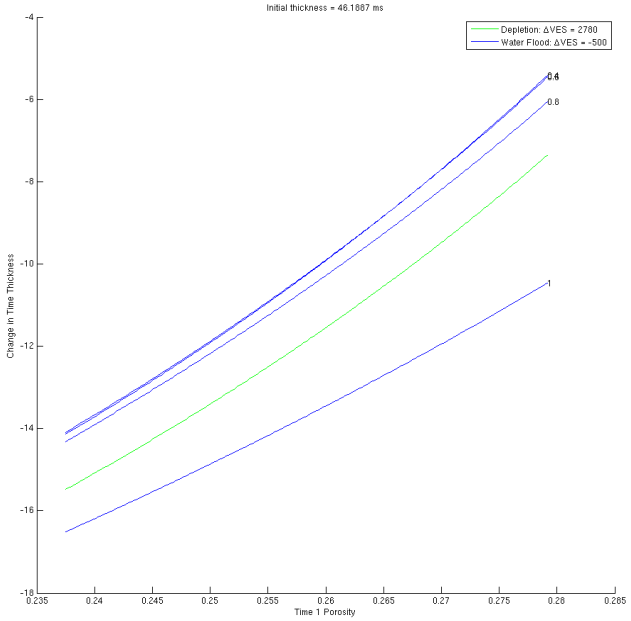

Fig 17: Change in time thickness in milliseconds between T_0 and T_1 depleted and compressed reservoir shown in green. Change in time thickness between T_0 and T_2 water flooded reservoir shown in blue for various labeled final T_2 water saturations. Initial T_0 time thickness is approximately 46 milliseconds.

In regards to AVO behavior, all water saturation and compressibility cases exhibit a negative gradient. Figure 18 illustrates an example of the reflection coefficient versus angle for the lowest pore compressibility case, which results in a T_1 porosity of approximately 28%. Additional examples for other pore compressibility/porosity cases can be found in Appendix D. Figure 19(a) shows a positive reflectivity at normal incidence for the 100% water saturation case when T_1 porosity is less than 27%, corresponding with class IIp AVO behavior. Additionally, positive reflectivity at normal incidence can be expected when water saturation is 85% and porosity is 24% or less, and when water saturation is 95% and porosity is 25% or less.

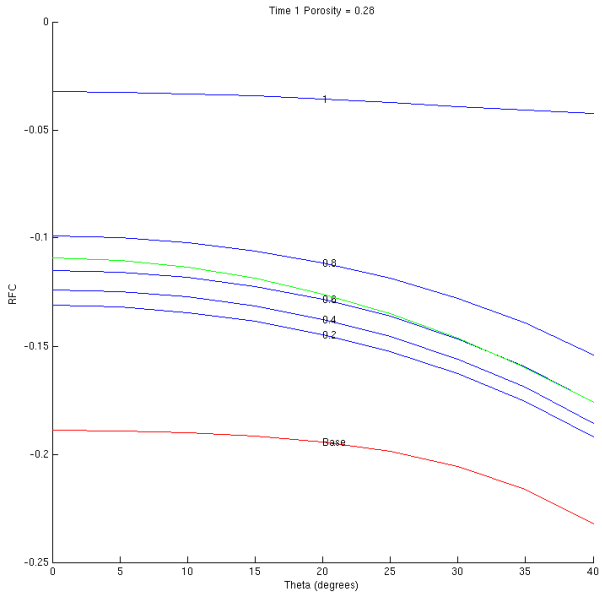

Fig 18: Reflection coefficient versus angle for the T_0 undepleted reservoir (red), the T_1 depleted and compressed reservoir (green), and the T_1 water flooded reservoir (blue) with labeled T_2 water saturations when T_1 porosity is 28%.

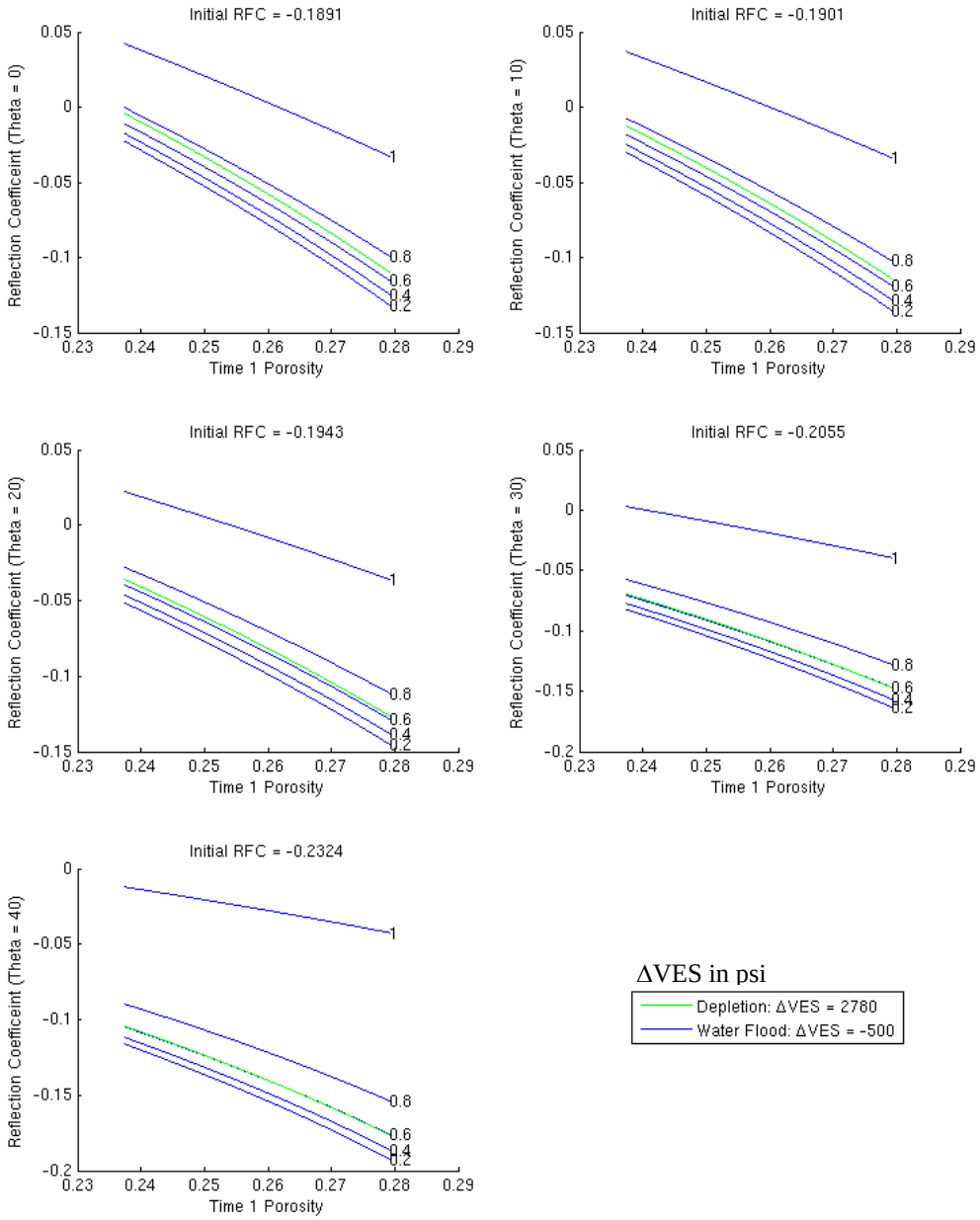

Fig 19: Reflection coefficient for angles 0 (a), 10 (b), 20 (c), 30 (d), and 40 (e) degrees versus T_1 porosity for the T_1 depletion case (green) and the T_2 water flood case (blue) for labeled T_2 water saturations. Initial T_0 reflectivity is listed for each angle case. The T_2 60% water saturation case for all porosity values looks very similar to the T_1 depletion case, especially at large angles of incidence.

Change in reflection coefficient for each angle with respect to T_1 porosity is included in Appendix D. Percent difference in reflection coefficient with respect to T_1 porosity is illustrated in Figure 20. When T_2 water saturation is 70%, close to 0% change in reflection coefficient is

seen at angles of 10 degrees and less. When T_2 water saturation is 60%, close to 0% change in reflection coefficient is seen at angles of 30 degrees and higher. So, if water saturation changes from a T_1 value of 20% to a T_2 value of 60% to 70% during water flooding, it is possible for nearly a 0% percent difference in reflection coefficient to be observed. In Figure 6, a negative percent difference means that the reflectivity has increased from T_1 to T_2, or the reservoir has acoustically hardened. A positive percent difference in reflection coefficient means the reflectivity has decreased from T_1 to T_2, or the reservoir has acoustically softened. Percent difference in reflection coefficient is calculated by

$$\text{Percent difference} = (RFC_2 - RFC_1)/RFC_2$$

where subscripts 1 and 2 refer to time steps 1 and 2, respectively.

The asymptotic behavior shown for the percent difference in the normal incident reflection coefficient in Figure 20(a) around the T_1 porosity value of 24% results from division of the difference in reflection coefficient by the small T_2 initial normal incident reflection coefficient as shown in Figure 19(a). Regardless of the initial compressibility, the largest percent difference in reflection coefficient can be seen at small angles. The largest change will be seen for the highest compressible sands with a small increase in water saturation. As previously stated, if water saturation increases to between 60% and 70% during water flooding, a very small change in reflection coefficient is observed, especially for the least compressible sands.

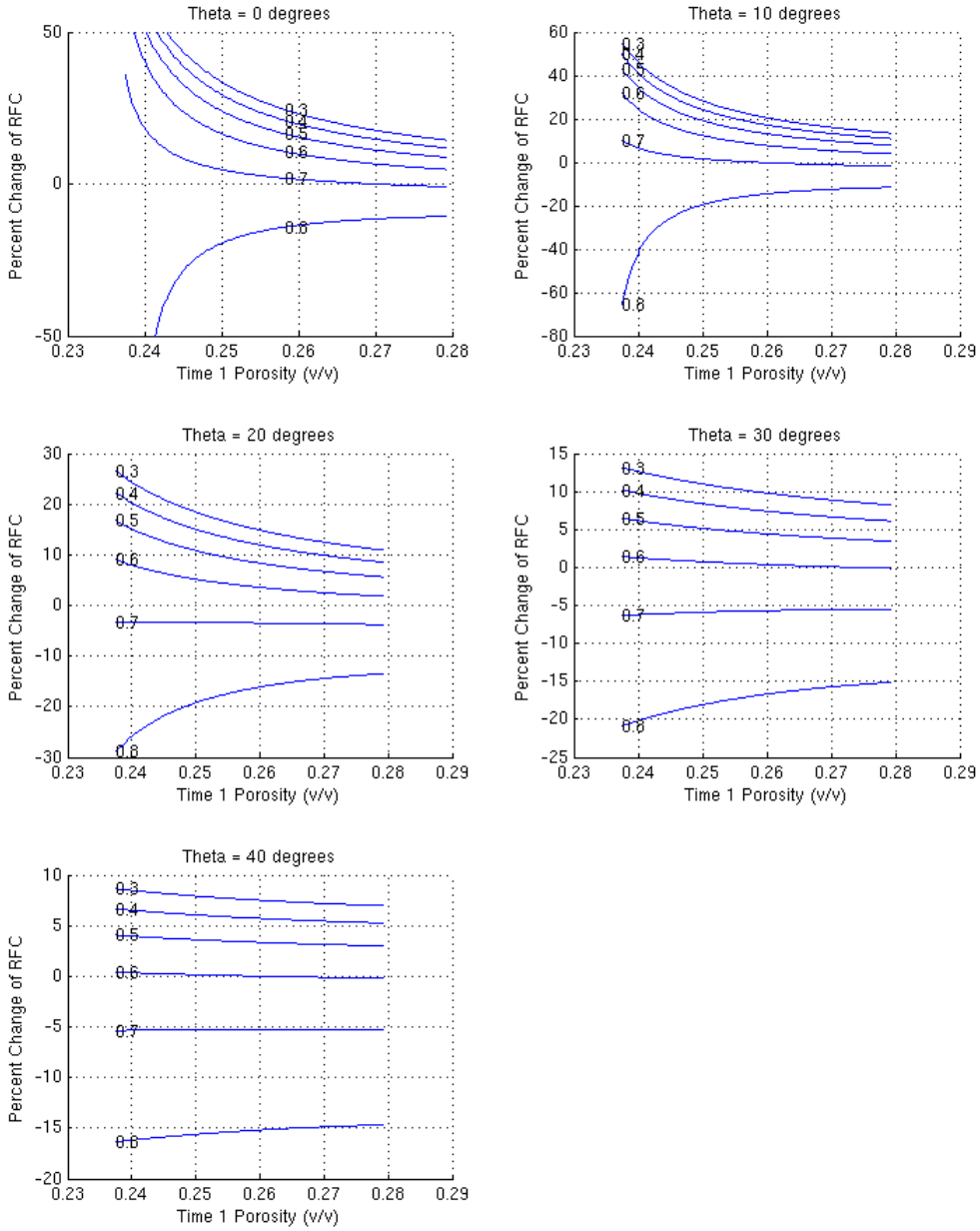

Fig 20: Percent difference in reflection coefficient between the T_1 depleted and compressed reservoir and the T_2 water flooded reservoir for various labeled final T_2 water saturations.

Gulf of Mexico Field Example

Eight years after initial production of a Gulf of Mexico gas reservoir began, a monitor survey was conducted over the field to analyze reservoir compaction and water movement. Plans

were in place to drill another well to increase production rates, and the seismic data acquired during the monitor survey were to be used to guide this well planning. A team of geophysicists compared 3D baseline and 2D monitor seismic datasets, and found evidence of reservoir compaction and shale expansion due to depletion. Water movement was recognized as a possibility, however, the limited 2D survey does not allow for analysis of spatial features. The planned well was drilled, and a dry hole resulted. Expected water saturation was 20%, but the actual water saturation was 60%.

This field example study will help answer two questions. First, would there be a noticeable change in time thickness and amplitude between the baseline seismic and monitor seismic for water saturation cases of 20% and 60%? Second, would it have been possible to differentiate between these two water saturation cases in the monitor seismic data?

The reservoir model and rock property model already utilized in the depletion methods study describe the geologic and acoustic components of this Gulf of Mexico field where the dry hole was drilled. As modeled in the primary depletion with weak aquifer support section, pore pressure has decreased by approximately 2800 psi between the base and monitor survey times. Compressional and shear velocity stress coefficients are 0.18 ft/s/psi, initial expected porosity is 30%, and the expected pore compressibility ranges from 25 to 75 μcips. Unfortunately, a full suite of log data was not collected in the dry hole, so compressed porosity is uncertain, and the pore compressibility uncertainty range cannot be reduced.

Using previously described formulas, we compare the change in acoustic properties from the base case of 20% water saturation and 30% porosity to the compacted monitor cases of 20% water saturation and 60% water saturation. Here, we specifically examine base and monitor time

thickness, normal incidence reflection coefficients, and normal incidence synthetic seismic amplitudes.

Initial predicted time thickness is approximately 46 ms. After compaction, final predicted time thickness ranges from 28 to 39 milliseconds, depending on velocity stress coefficients and water saturation. With this range in magnitude of change in time thickness, it is expected that a decrease in time thickness between base and monitor seismic at the reservoir will be visible. Similar results are seen for the other velocity stress coefficients examined in this test and plotted in Figure 21 for sake of comparison. Figure 22 shows the change in time thickness from the base to the monitor cases for various compacted porosity and velocity stress coefficients.

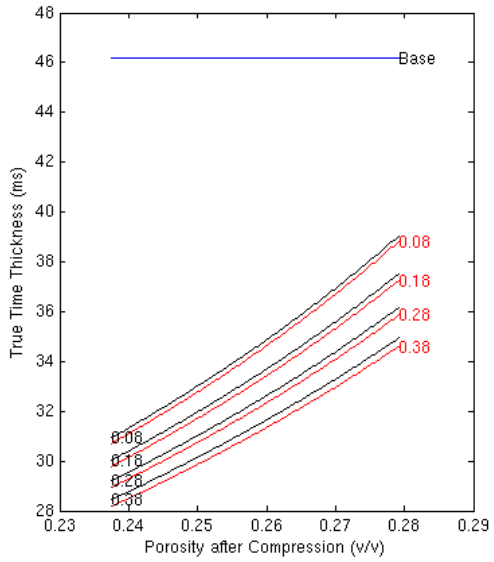

Figure 21: Time 1 time thickness versus time 1 monitor compacted porosity for water saturation values of 20% (red) and 60% (black). Velocity stress coefficients (ft/s/psi) are labeled. Baseline case (blue) is plotted for reference.

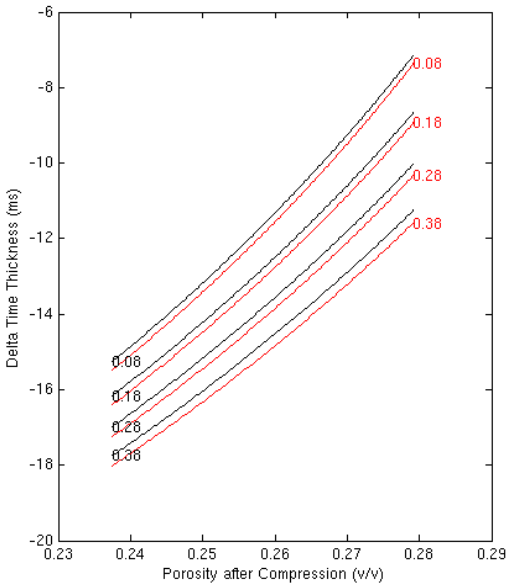

Figure 22: Change in time thickness between baseline time 0 and monitor time 1 for monitor time 1 saturation values of 20% (red) and 60% (black). Velocity stress coefficients (ft/s/psi) are labeled. Negative values for change in time thickness indicate a decrease in time thickness.

Seismic time thickness in the actual base seismic ranges from 40 to 48 milliseconds in thick reservoir sections. In these areas, the difference between monitor and base seismic loop thickness ranges from 0 ms to 5 ms. This change in loop thickness is smaller than the predicted change in loop thickness, which has a minimum of 7 milliseconds. The predicted change in loop thickness could be larger than the actual change in loop thickness perhaps because the predicted velocity after compaction is too low and/or the modeled compacted reservoir thickness is larger than the actual reservoir (i.e., modeled pore compressibility cases are too high).

Figure 23 shows the difference of the predicted change in time thickness between the two monitor cases with 20% water saturation and 60% water saturation. Comparison of the predicted monitor time thickness cases shows that the compacted 20% water saturation case is not easily distinguishable from the compacted 60% water case. With a velocity stress coefficient of 0.18 ft/s/psi, the difference in time thickness between the compacted 20% water saturation and 60%

water saturation cases is approximately ¼ of a millisecond, for all porosity/pore compressibility cases. As seen on Figure 23, the largest time difference of 0.33 milliseconds between the 20% and 60% water saturation cases results when the highest compacted porosity (lowest pore compressibility) is paired with the largest velocity stress coefficient. With such a small differences in time thickness, it would be very difficult, if not impossible, to differentiate between the compacted 20% water saturation case and the 60% water saturation case when examining seismic loop time thickness as the uncertainty in the seismic loop thickness can exceed 1 millisecond.

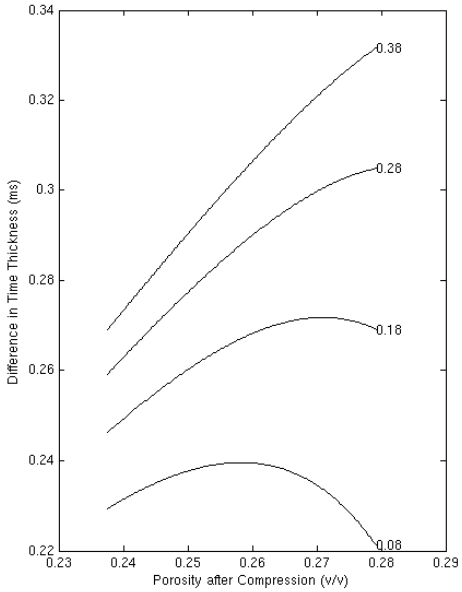

Figure 23: Difference between time 1 monitor thickness values for water saturation cases of 20% and 60%. Velocity stress coefficients (ft/s/psi) are labeled.

The predicted normal incidence reflection coefficient for the baseline case is approximately –0.18, while the predicted monitor case ranges from –0.12 to +0.05, depending on velocity stress coefficients and compacted porosity. In addition to the normal incidence reflection coefficient, Figure 24 illustrates the reflection coefficients for various angles for the base case and the two monitor cases considered, which all exhibit Class III AVO behavior. With

this range in the magnitude of change in the normal incidence reflection coefficient, it is expected that a change in amplitude between base and monitor seismic in the reservoir will be visible. With minimum compaction, the normal incidence reflection coefficient is expected to change by 40% or 50% for stress coefficients of 0.08 and 0.18 ft/s/psi. Percent change in reflection coefficient can be seen in Figure 25, where the percent change is equal to $\Delta RFC/RFC_1$.

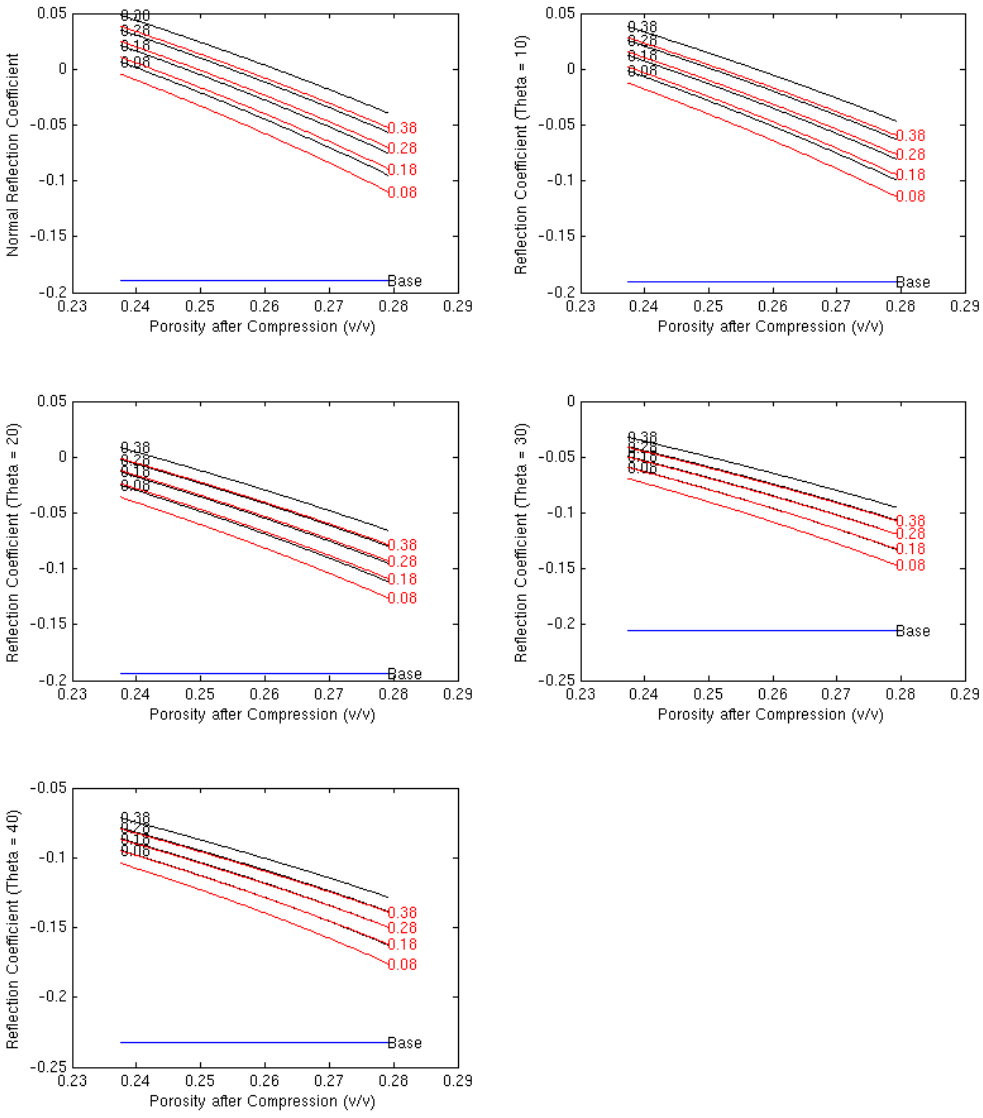

Figure 24: Time 1 reflection coefficient for angles of incidence of a) 0 b) 10 c) 20 d) 30 e) 40 degrees versus time 1 monitor compacted porosity for water saturation values of 20% (red) and 60% (black). Velocity stress coefficients (ft/s/psi) are labeled. Baseline case (blue) is plotted for reference.

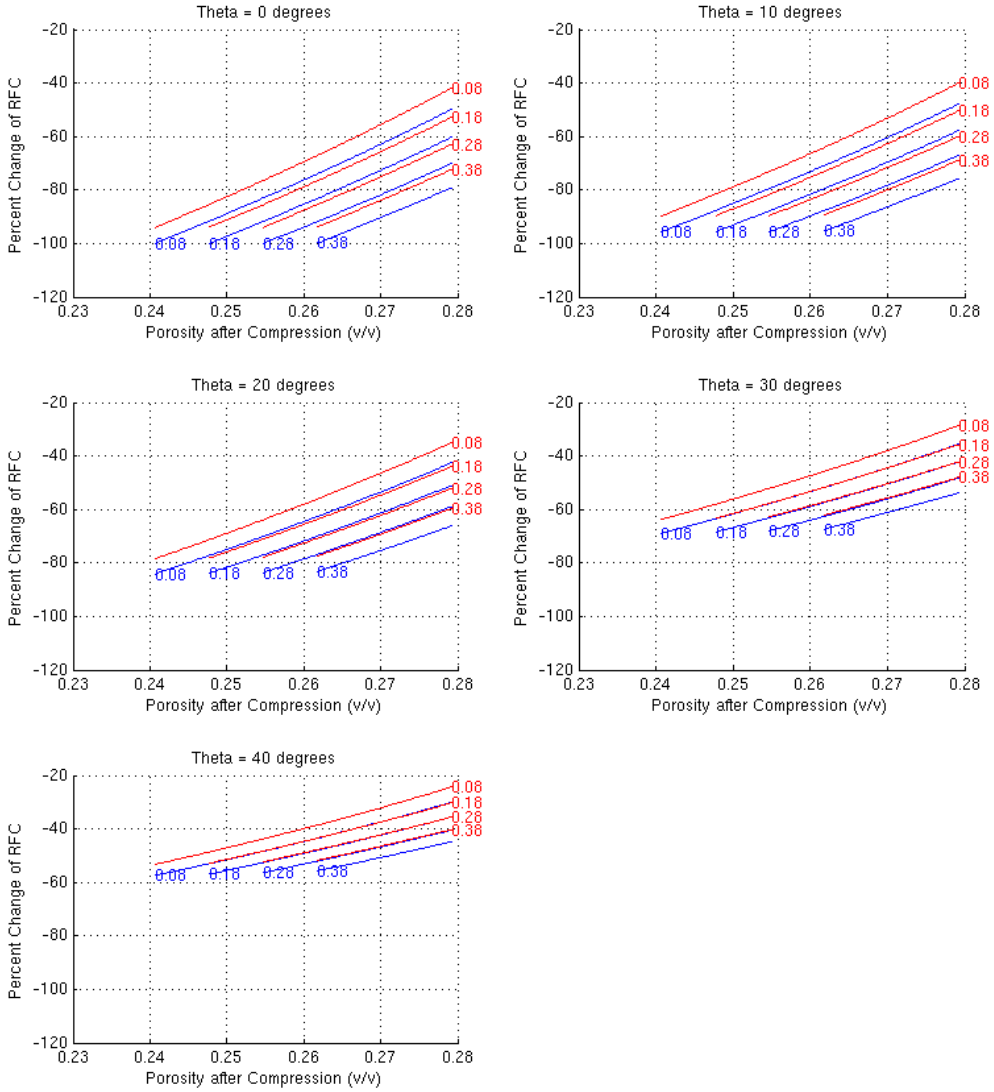

Figure 25: Percent change in reflection coefficient for angles of incidence of a) 0 b) 10 c) 20 d) 30 e) 40 degrees between baseline time 0 and monitor time 1 versus monitor time 1 compacted porosity for monitor time 1 saturation values of 20% (red) and 60% (blue). Velocity stress coefficients (ft/s/psi) are labeled.

We convolved the baseline and two monitor reflectivity series with a 40-Hz Ricker wavelet, and applied a 90^{o} phase shift to the resulting normal incidence synthetic seismic data. The differences in amplitude between the baseline and the two monitor synthetic seismic datasets were computed. The amplitude difference between the baseline synthetic seismic and monitor

20% water saturation case ranges from 32% to 100%, depending on compacted porosity and velocity stress coefficients. The amplitude difference between the baseline synthetic seismic and the monitor 60% water saturation case ranges from 40% to 100%, depending on compacted porosity and velocity stress coefficients. Figures 26 and 27 show the percent change in amplitude between the baseline synthetic seismic and the monitor synthetic seismic cases with water saturation of 20% and 60%, respectively.

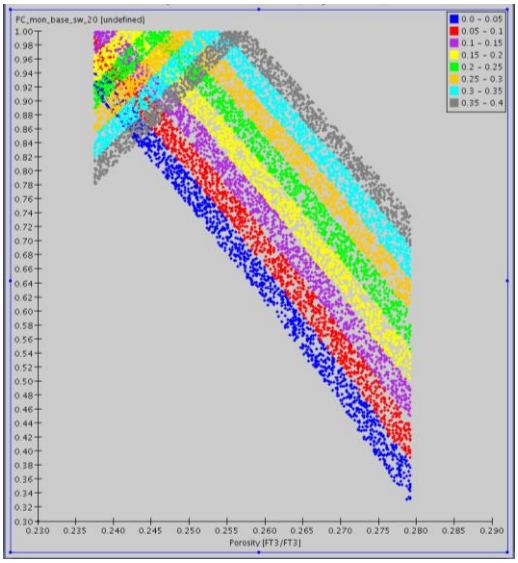

Figure 26: Fractional difference in normal incidence synthetic seismic amplitude between the time 0 baseline case and time 1 monitor water saturation case of 20% versus time 1 compacted porosity. Z-value colors represent velocity stress coefficients ranging from 0 ft/s/psi (blue) to 0.40 ft/s/psi (grey). Percent change values can be obtained by multiplying y-axis by 100.

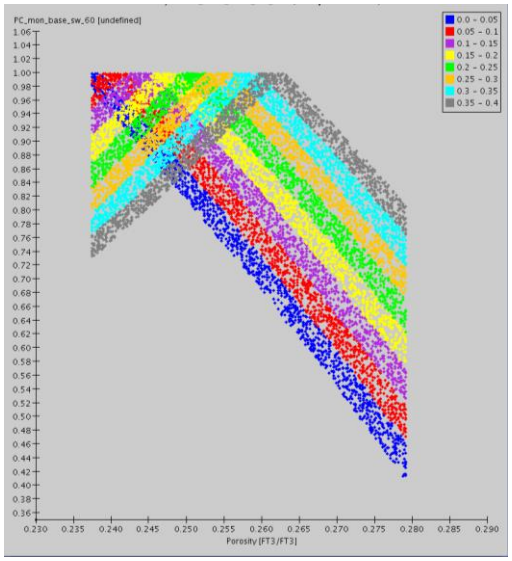

Figure 27: Fractional difference in normal incidence synthetic seismic amplitude between the time 0 baseline case and the time 1 monitor water saturation case of 60% versus time 1 compacted porosity. Z-value colors represent velocity stress coefficients ranging from 0 ft/s/psi (blue) to 0.40 ft/s/psi (grey). Percent change values can be obtained by multiplying y-axis by 100.

For the real seismic data acquired at this Gulf of Mexico field, the decrease in amplitude between the baseline and monitor nearstack seismic data is 16% to 40% (Figure 28). The largest decrease in real seismic amplitude at 40% is associated with an area where compaction and water influx were expected to have occurred. If the water saturation in this area is 60%, our modeling would suggest that the velocity stress coefficient is very low (less than 0.05 ft/s/psi) and the compacted porosity is about 28% (Figure 27), which corresponds to the low pore compressibility case of 25 μcips. Note that this velocity stress coefficient of 0.05 ft/s/psi is much lower than the expected velocity stress coefficient of 0.18 ft/s/psi for this field.

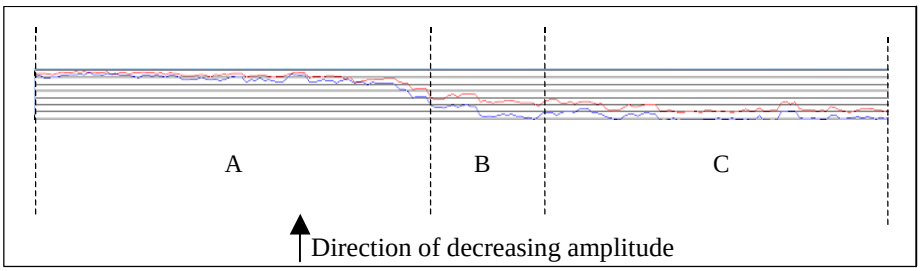

Figure 28: Amplitude extraction from baseline seismic data (blue) and monitor seismic data (red). Amplitude decreases by 40% in area where compaction and water influx was expected (B) and 16% where only compaction was expected (C). Aquifer section shows little change in amplitude (A). Horizontal axis shows the position along the seismic line.

Outside of the aquifer area, the smallest decrease in the real seismic amplitude at 16% is associated with an area where only compaction is believed to have occurred. Since no water influx is expected here, the estimated water saturation is 20%. According to the previous paragraph, the coupling of the velocity stress coefficient of less than 0.05 ft/s/psi along with a compacted porosity of 28% and a 60% water saturation can provide a match to the actual seismic amplitude reduction of 40% in the area where compaction and water influx was expected. However, the coupling of the same velocity stress coefficient and compacted porosity with a water saturation of 20% gives us an expected change in amplitude of 32% (Figure 26). This predicted change in amplitude of 32% is twice as large as the actual change in amplitude of 16%. Thus, we do not have a modeled pair of velocity stress coefficients and compacted porosities that would match both the 16% seismic amplitude reduction/20% water saturation case and the 40% seismic amplitude reduction/60% water saturation case.

Furthermore, we have not modeled a 20% water saturation case that would result in a change in amplitude of 16% since our minimum predicted change in amplitude is 32%. Some possible reasons for the predicted change in amplitude at 32% being larger than the actual change in amplitude at 16% include 1) model pore compressibility is too high, 2) model pressure

decrease is too large, 3) model thickness is too high, 4) all tested stress velocity coefficients are too large, 5) lack of repeatability between seismic surveys (3D baseline and 2D monitor data were acquired over five years apart), 6) lack of shale expansion in the model. To further address reason 5, if the shales in the model were allowed to expand, the shale after reservoir depletion/compression would be acoustically softer, thus the contrast between the expanded shale and compressed reservoir would be smaller. This would decrease the reflection coefficient and amplitude, however the effects of the shale expansion are not expected to be significant. It is also possible that the actual reduction in amplitude and the predicted reduction in amplitude do not match for both the sections B and C of Figure 28 because perhaps sections B and C do not have 60% and 20% water saturations as expected.

To determine if it is possible to see a difference between the two saturation cases in the monitor data, we compare the two monitor saturation cases. The compacted 20% water saturation case is somewhat distinguishable from the compacted 60% water case when considering the normal incidence reflection coefficient. The difference between these two reflection coefficient cases ranges from 0.008 to 0.015, depending on velocity stress coefficients and compacted porosity. Figure 29 shows the difference in reflection coefficient between the two monitor saturation cases for the compacted porosity and velocity stress coefficients used in this study.

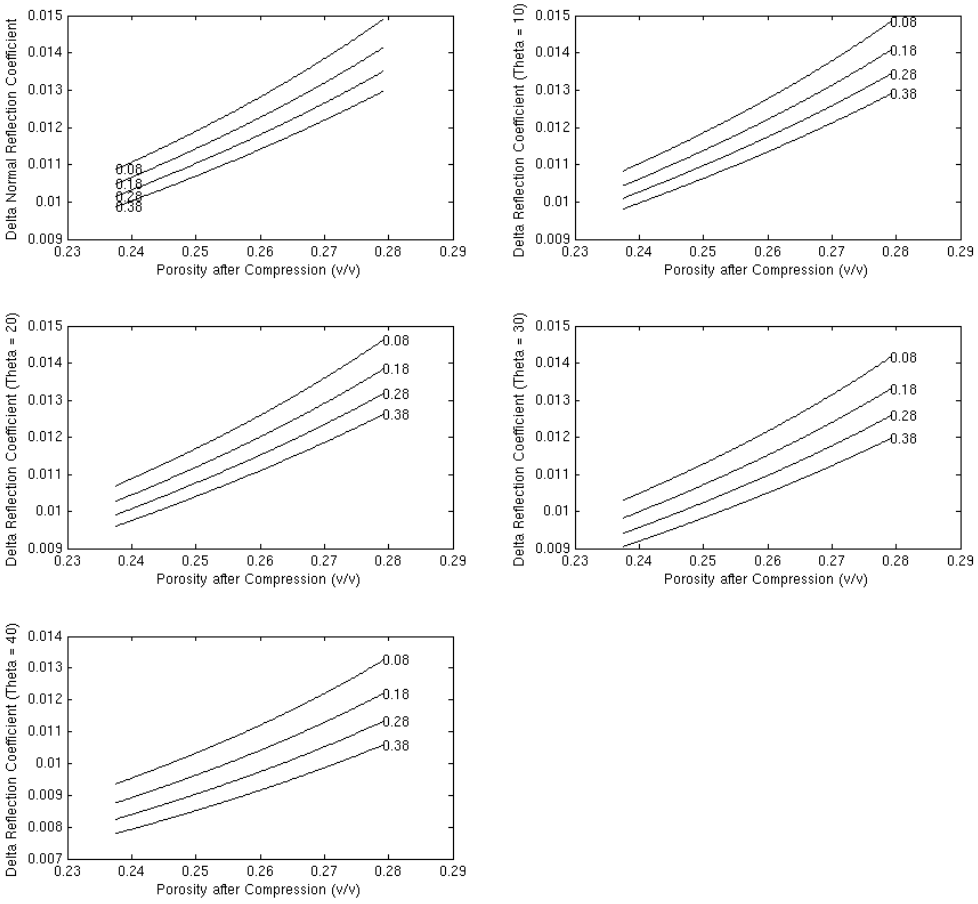

Figure 29: Difference in reflection coefficient for angles of incidence of a) 0 b) 10 c) 20 d) 30 e) 40 degrees between monitor time 1 water saturation cases of 20% and 60% versus monitor time 1 compacted porosity. Velocity stress coefficients (ft/s/psi) are labeled.

When comparing synthetic seismic amplitudes of the two monitor saturation cases (Figure 30), the largest percent change in amplitude is 24%. This 24% change occurs when the smallest velocity stress coefficient used in the study at 0 ft/s/psi is paired with the smallest pore compressibility at 25 μcips. In this study, the pressure change between base and monitor cases resulted in porosity decreasing from 30% to just under 28% with a pore compressibility of 25 μcips. For this particular field, the expected velocity stress coefficient is 0.18 ft/s/psi. This velocity stress coefficient results in a percent change in amplitude ranging from 6% to 15% with

pore compressibilities of 75 μcips and 25 μcips (or compacted porosity of 24% to 28%), respectively.

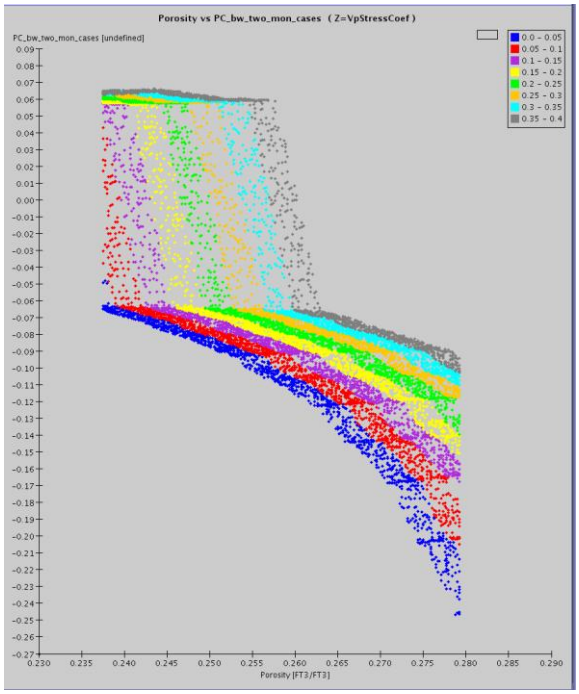

Figure 30: Fractional difference in normal incident synthetic seismic amplitude between the two time 1 monitor water saturation cases of 20% and 60% versus time 1 compacted porosity. Z-value colors represent velocity stress coefficients ranging from 0 ft/s/psi (blue) to 0.40 ft/s/psi (grey). Percent change values can be obtained by multiplying y-axis by 100.

If the noise level in the acquired monitor seismic data is higher than the expected percent change in amplitude between these two predicted monitor cases, it probably would not be possible to distinguish the 20% water saturation case from the 60% water saturation case. In the near-angle monitor seismic data, the fluctuation of the amplitude in the hydrocarbon-bearing portion of the reservoir is approximately 15%. This is higher than the expected percent change in amplitude between the two water saturation cases for the expected velocity stress coefficient of 0.18 ft/s/psi and the entire range of expected pore compressibilities. Thus, due to the noise level in the monitor seismic data, it is unlikely that it would have been possible to distinguish between

the 20% water saturation and 60% water saturation cases using monitor seismic amplitudes with this Gulf of Mexico gas reservoir.

In summary, this study predicts that there would be a noticeable change in seismic loop thickness and amplitude between baseline and monitor seismic datasets when the reservoir compacts and monitor water saturation remains at 20% or increases to 60%. However, when looking at the monitor seismic dataset, it would be difficult to distinguish between a 20% water saturation case and a 60% water saturation case. This difference in water saturation would be more apparent for less compressible sands as the higher the compacted porosity, the larger the amplitude difference between the 20% and the 60% water saturation cases. For the expected velocity stress coefficient of 0.18 ft/s/psi in this particular gas reservoir, the two water saturation cases would not be distinguishable as the difference in amplitude is not above the noise level present in the monitor seismic data. However, the rock physics modeling does not produce synthetic amplitude changes that are in agreement with the measured amplitude changes at the expected pore pressure decrease and water saturation change. These mismatches suggest that this field-specific rock property model requires improvement in the pressure-variant sense and/or the changes in actual seismic amplitudes are associated with pressure/porosity, thickness, or saturation cases that were not modeled.

Suggested further studies include refining rock physics modeling trends by calibrating synthetics from repeat log data to monitor seismic data and reapplying the results to the reservoir model. Another subsequent study could include allowing for bounding shale expansion in time-lapse modeling. Additionally, similar modeling could be applied to other fields to improve understanding of time-lapse responses.

References

Avseth, P., Mukerji, T., and Mavko, G., 2005, Quantitative Seismic Interpretation, Cambridge, United Kingdom, Cambridge University Press, p. 1-46, 168-203.

Batzle, M., Christiansen, R., and Han, D-H., 1998, Reservoir recovery processes and geophysics: The Leading Edge, v. 17, p. 1444-1447.

Castagna, J. P., Batzle, M.L, and Eastwod, R.L., 1985, Relationships between compressional-wave and shear-wave velocities in clastic silicate rocks: Geophysics, v. 50, p. 571-581.

Castro, S. A., Caers, J., Otterlei, C., Meisingset, H., Hoye, T., Gomel, P., and Zachariassen, E., 2009, Incorporatine 4D seismic data into reservoir models while honoring production and geologic data: A case study: The Leading Edge, v. 28, p. 1498-1506.

Fanchi, J.R., 2001, Time-lapse seismic monitoring in reservoir management: The Leading Edge, v. 20, p. 1140-1147.

Gassmann, F., 1951, Elastic waves through a packing of spheres: Geophysics, v. 16, 673-685.

Han, De-hua, Nur, A., and Morgan, D.,1986, Effects of porosity and clay content on wave velocities in sandstones: Geophysics, v. 51, p. 2093-2107.

Herwanver, J.V., and Horne, S. A., 2009, Linking reservoir geomechanics and time-lapse seismics: Predicting anisotropic velocity changes and seismic attributes: Geophysics, v. 74, p. W13-W33.

Holt, R. M., Nes, O., and Jaer, E. F., 2005, In-situ stress dependence of wave velocities in reservoir and overburden rocks: The Leading Edge, v. 24, p. 1268-1274.

Lumley, D. E., 2004, Business and technology challenges for 4D seismic reservoir modeling: The Leading Edge, v. 23, p. 1166-1168.

Shuey, R. T., 1985, A simplification of the Zoeppritz equations: Geophysics, v. 50, 609-614.

Tura, A., Hohl, D., Bourne, S., Moen, R., Nutbrown, R., Thomas, M., and Lanson, T., 2006, Feasibility of monitoring compaction and compartmentalization
using 4D time shifts and seafloor subsidence: The Leading Edge, v. 25, p. 1169-1175.

Wang, Z., 2001, Fundamentals of seismic rock physics: Geophysics, v. 66, p. 398-412.

Wood, D. M., 1990, Soil Behavior and Critical State Soil Mechanics: Cambridge, United Kingdom, Cambridge University Press, p. 94-95.

Appendix A- Supplementary Plots For Depletion With Strong Aquifer Support

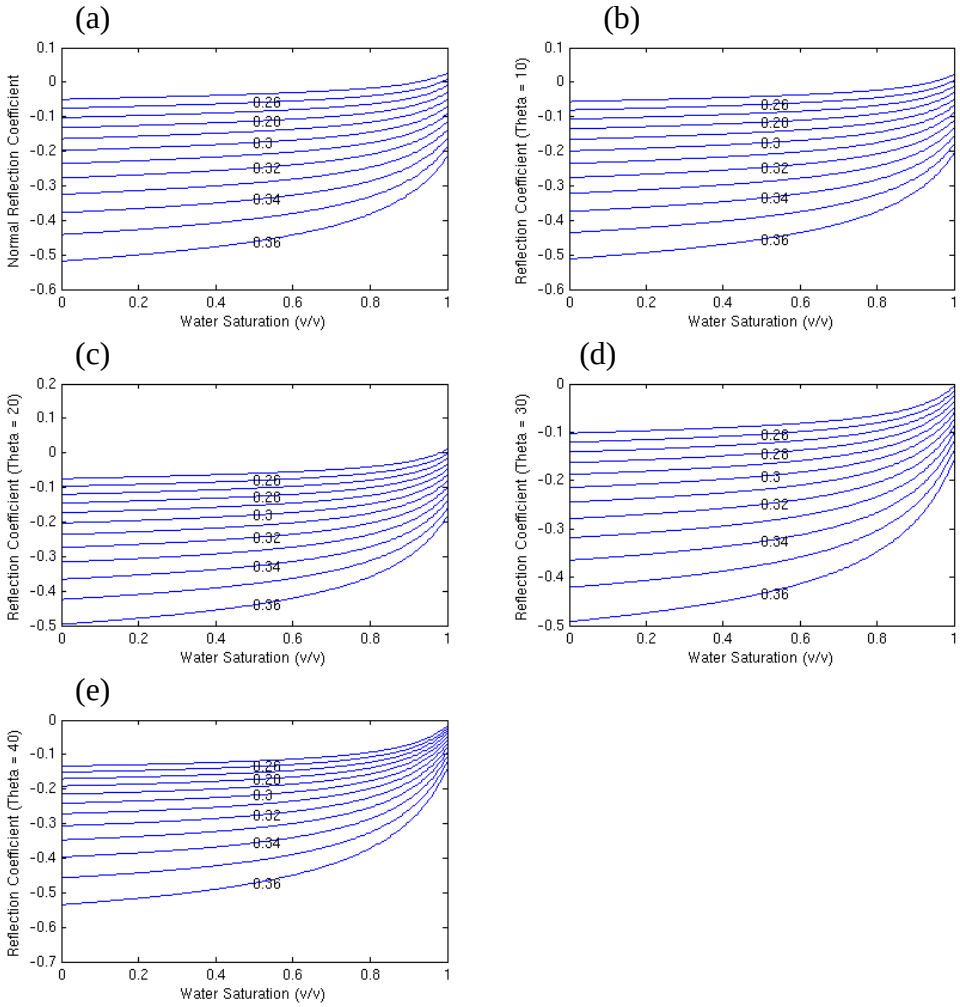

Figure A-1: A cross plot of water saturation versus reflection coefficient is provided for the normal incidence reflection and for reflection angles of 10, 20, 30, and 40 degrees. The contour lines on each plot represent the labeled porosities.

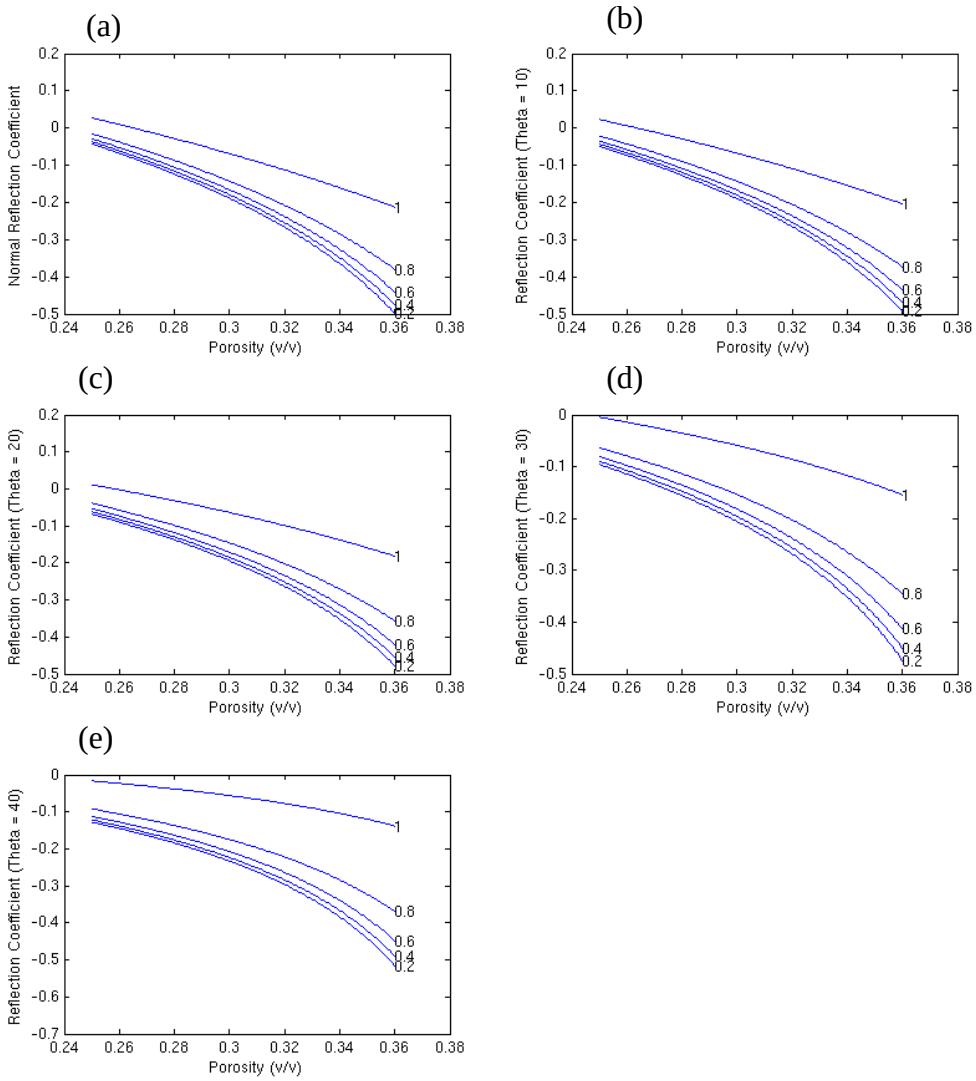

Figure A-2: Reflection coefficient for porosites (x-axis) ranging from 25% to 36% Incidence angles are 0 (a), 10 (b), 20 (c), 30 (d), and 40 (e) degrees. Water saturation cases are shown as contours in each plot ranging form 25% to 36%.

Appendix B: Change In Reflection Coefficient For Depletion With Aquifer Support

We are interested in how the reflection coefficient changes as water saturation increases while the reservoir is depleted. The change in reflection coefficient is given by

$$\Delta RFC = RFC_2 - RFC_1.$$

We give a convenient look-up table in the form of a cross plot for normal incidence change in reflection coefficient (Figure B-1) and provide a usage example to determine the change in normal incident reflection coefficient when the water saturation increases from 20% to 60% for a porosity of 34%. Initial water saturations are the labeled curves. For this example, the change in water saturation is 40%. Find the initial water saturation curve of 20% (with black arrow) on the upper left hand plot associated with 34% porosity in blue. Trace the curve down until reaching the delta saturation value of 40% on the x–axis. The corresponding change in reflection coefficient can be read from the y-axis. For this example, the change in normal incident reflection coefficient is approximately 0.04. A positive change in reflection coefficient means that the reflection coefficient value is increasing, or becoming less negative. The magnitude of the reflection coefficient is decreasing. Figure B-2 gives the same look-up table in a cross plot form for angle of incidence 0, 10, 20, 30, and 40 degrees. We can see that a change in water saturation results in a larger change in reflection coefficient for all angles of incidence when porosity is high.

The percent difference of reflection coefficient is given by

$$\text{Percent difference} = \Delta RFC/RFC_2.$$

The percent difference in reflection coefficient for these three porosity cases can be found in plots B-3, B-4, and B-5. For the example in the preceding paragraph, the percent difference of normal incident reflection coefficient is 10%. The percent difference in reflection coefficient is

small (less than 15%) unless the change in water saturation is very high. For instance, if the initial water saturation is 20%, water saturation would have to increase by at least 40% in order to have a change in normal incident reflection coefficient of at least 20%.

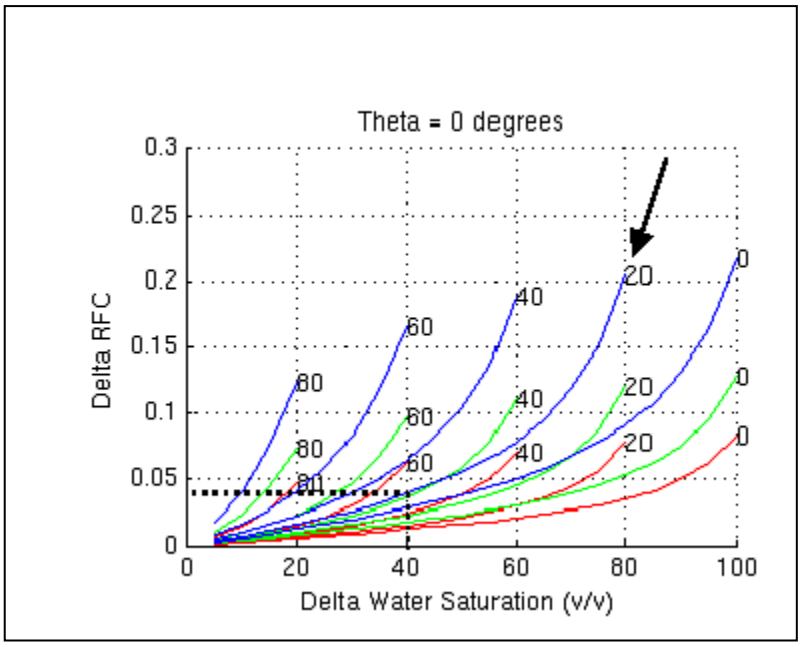

Figure B-1: Change in reflection coefficient as a function of change in water saturation. To determine change in reflection coefficient, identify initial water saturation curve. The black arrow points to the initial water saturation curve of 20% for the 34% porosity case. Locate the position where the desired change in water saturation on the x-axis intersects the initial water saturation curve. In this example, the change in water saturation is 40%, as water saturation is increasing from 20% to 60%. The resulting change in normal incident reflection coefficient can be read off the y-axis. In this example, the change in reflection coefficient is 0.04.

The contour colors represent different porosity values. Blue: 34% porosity, Green: 30% porosity, and Red: 26% porosity.

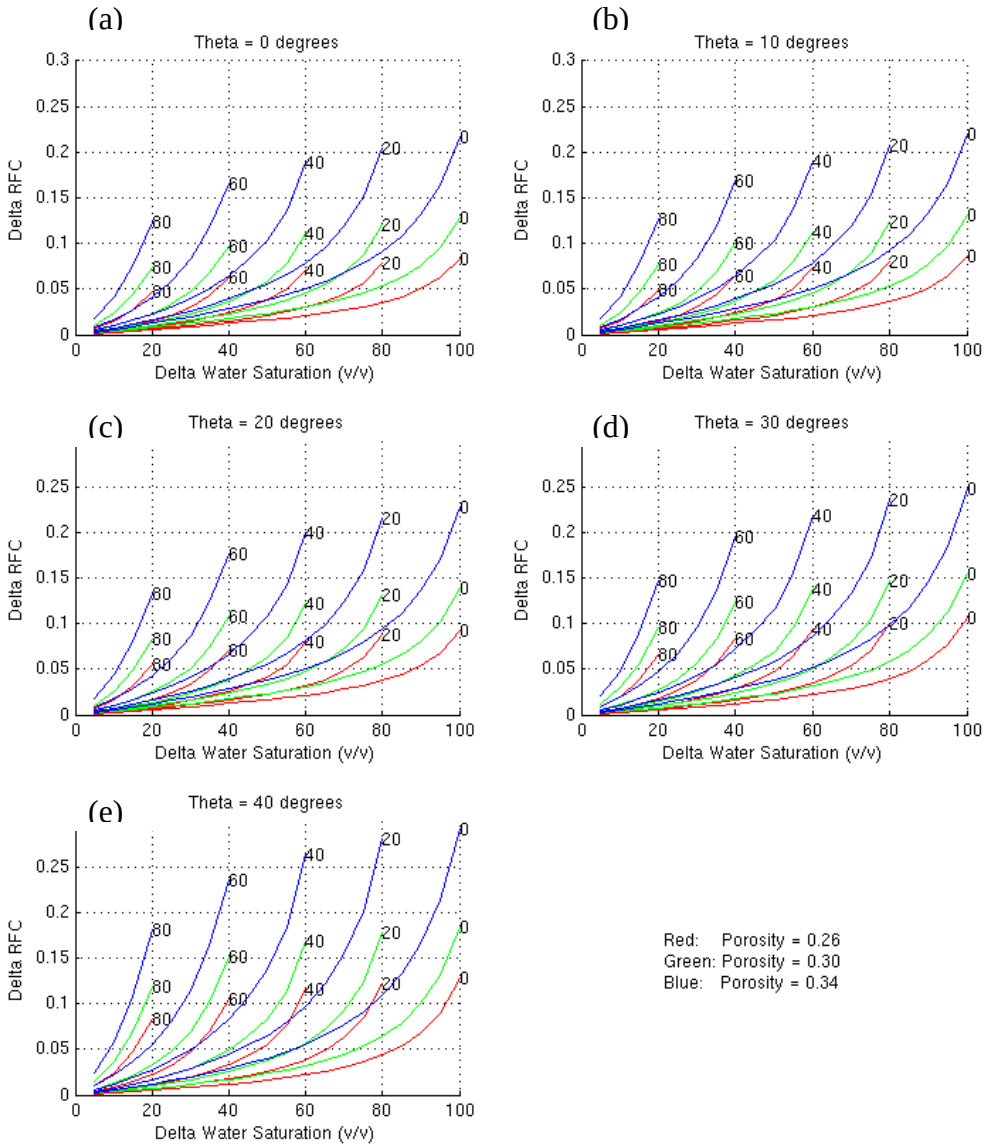

Figure B-2: Change in reflection coefficient as a function of change in water saturation for incidence angles 0, 10, 20, 30, and 40 degrees. For an example on how to read the plot, refer to the text for Figure B-1. Figure B-1(a) is the same as Figure B-1.

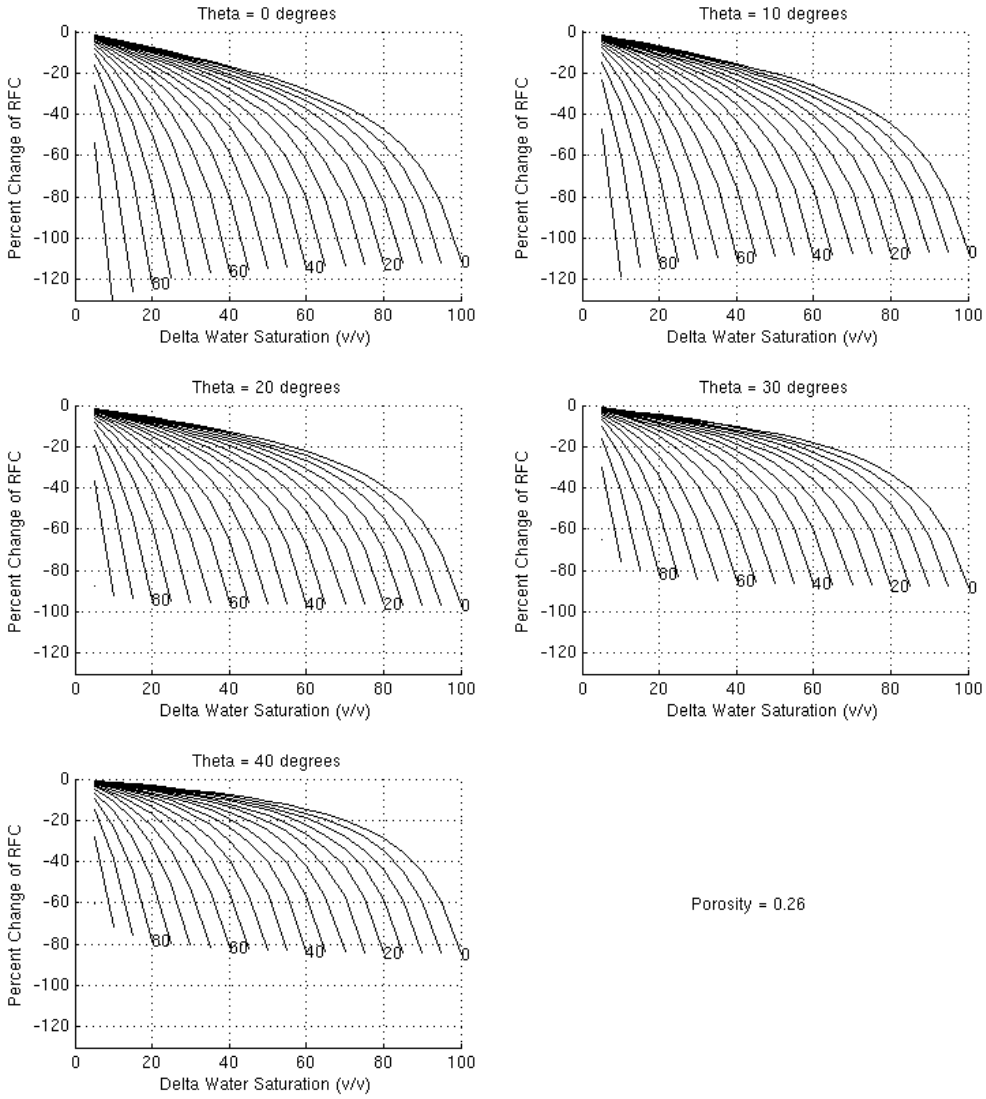

Figure B-3: Percent difference in reflection coefficient as a function of change in water saturation for incidence angles 0, 10, 20, 30, and 40 degrees. Porosity value is 26% in all plots.

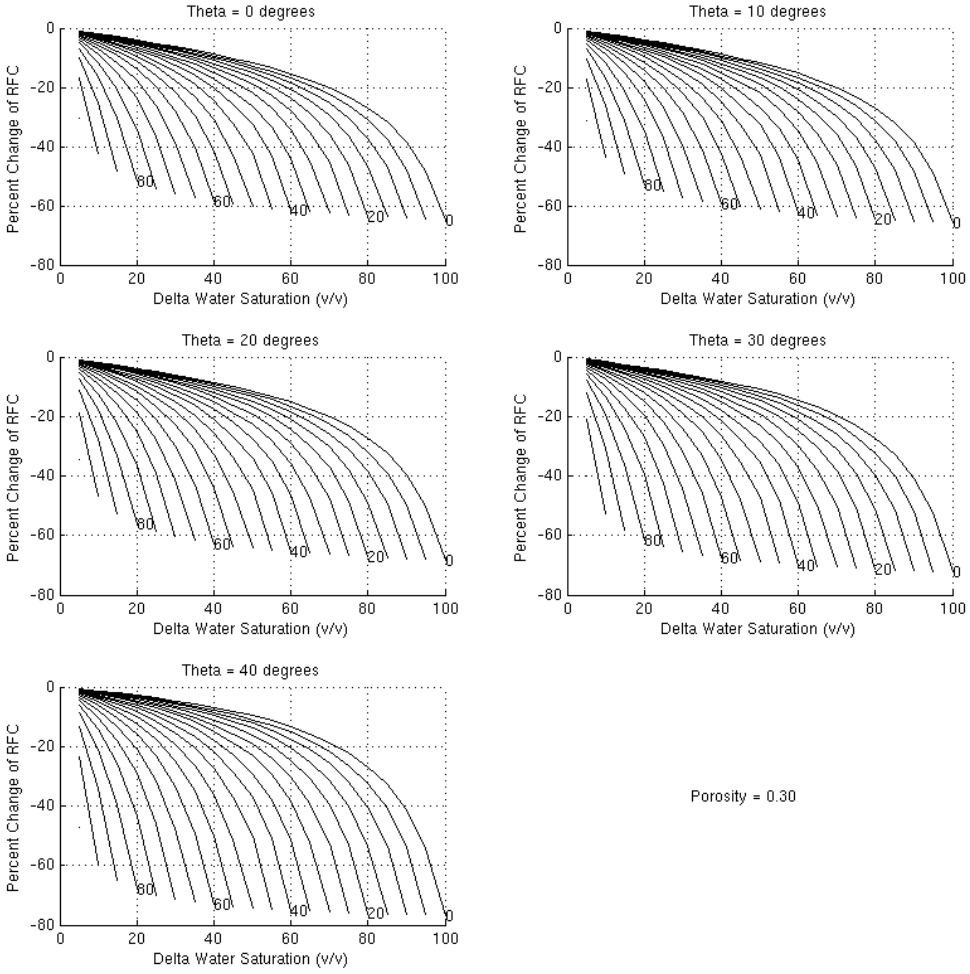

Figure B-4: Percent difference in reflection coefficient as a function of change in water saturation for incidence angles 0, 10, 20, 30, and 40 degrees. Porosity value is 30% in all plots.

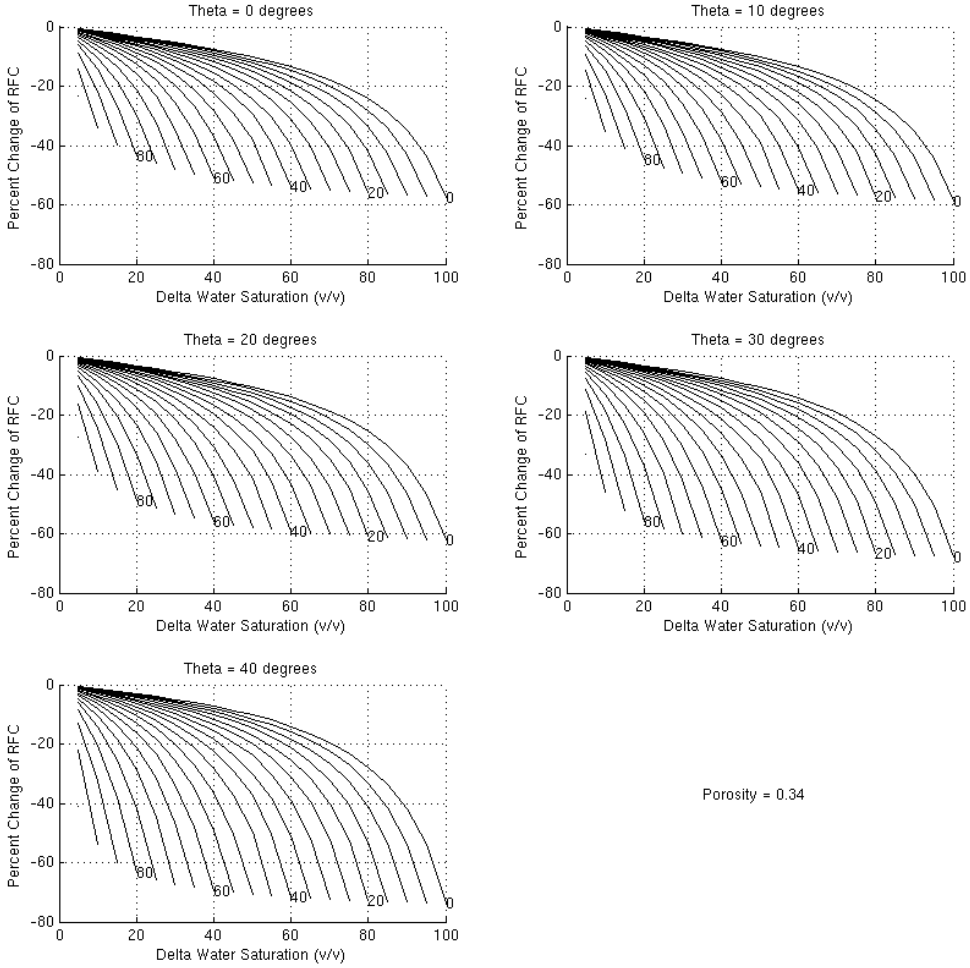

Figure B-5: Percent difference in reflection coefficient as a function of change in water saturation for incidence angles 0, 10, 20, 30, and 40 degrees. Porosity value is 34% in all plots.

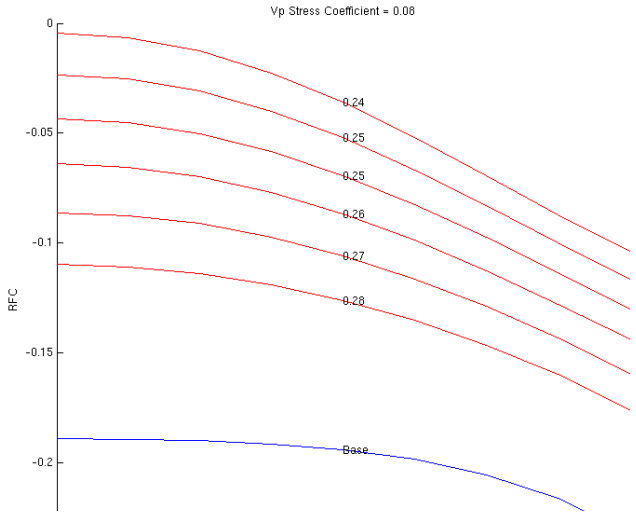

Figure C-1: AVO behavior of the reflection coefficients for final porosities after compaction (labeled contours) ranging from 24% to 28% when velocity stress coefficient is 0.08 ft/s/psi. Initial (base) case with porosity of 30% is shown as reference in blue.

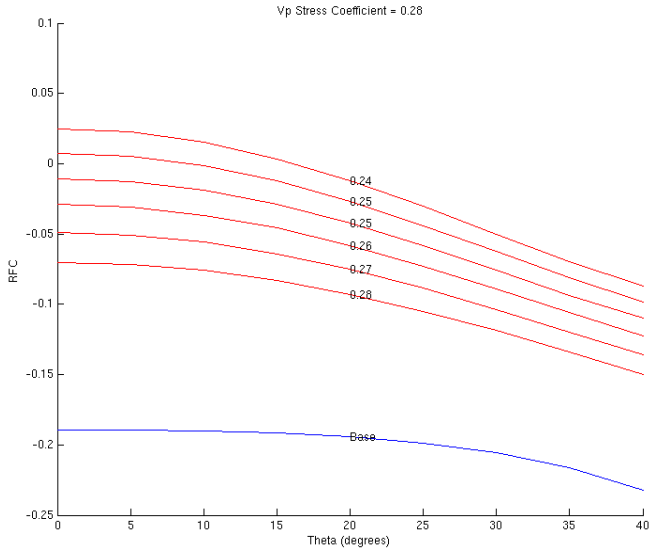

Figure C-2: AVO behavior for final porosities after compaction (labeled contours) ranging from 24% to 28% when velocity stress coefficient is 0.28 ft/s/psi. Initial (base) case with porosity of 30% is shown as reference in blue.

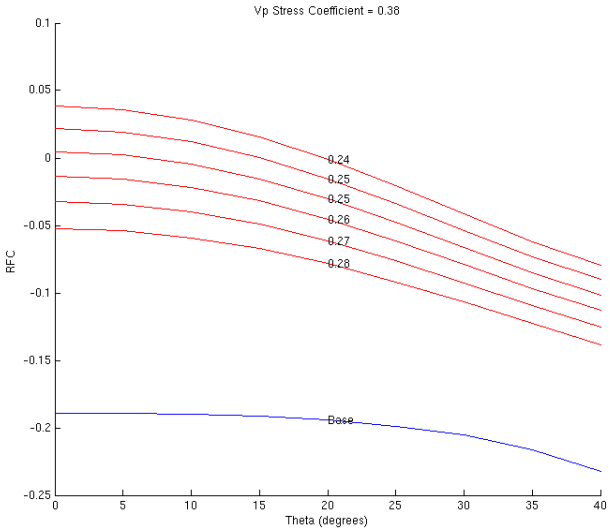

Figure C-3: AVO behavior of the reflection coefficients for final porosities after compaction (labeled contours) ranging from 24% to 28% when velocity stress coefficient is 0.38 ft/s/psi. Initial (base) case with porosity of 30% is shown as reference in blue.

Appendix D: Supplementary Plots For Water Flood Depletion

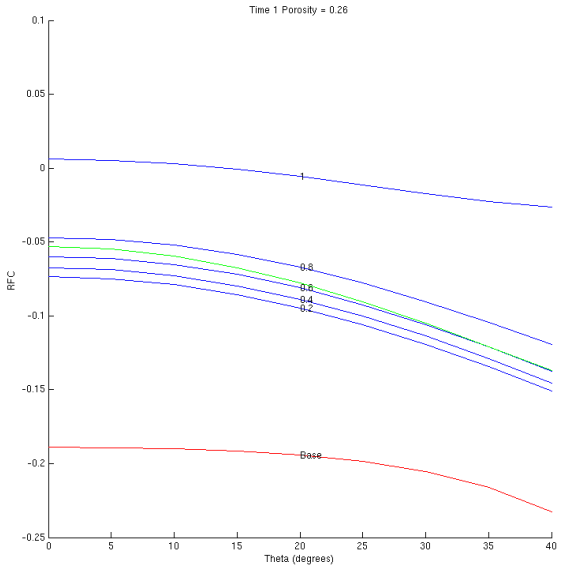

Figure D-1: Reflection coefficient versus angle for the T_0 undepleted reservoir (red), the T_1 depleted and compressed reservoir (green), and the T_1 water flooded reservoir (blue) with labeled T_2 water saturations when T_1 porosity is 26%.

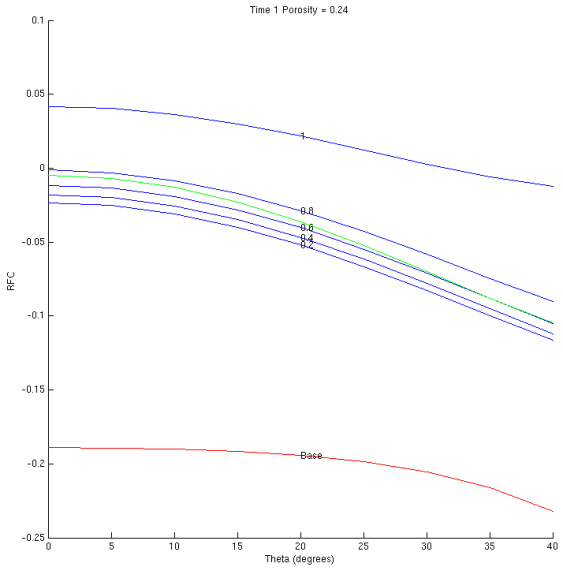

Figure D-2: Reflection coefficient versus angle for the T_0 undepleted reservoir (red), the T_1 depleted and compressed reservoir (green), and the T_1 water flooded reservoir (blue) with labeled T_2 water saturations when T_1 porosity is 24%.

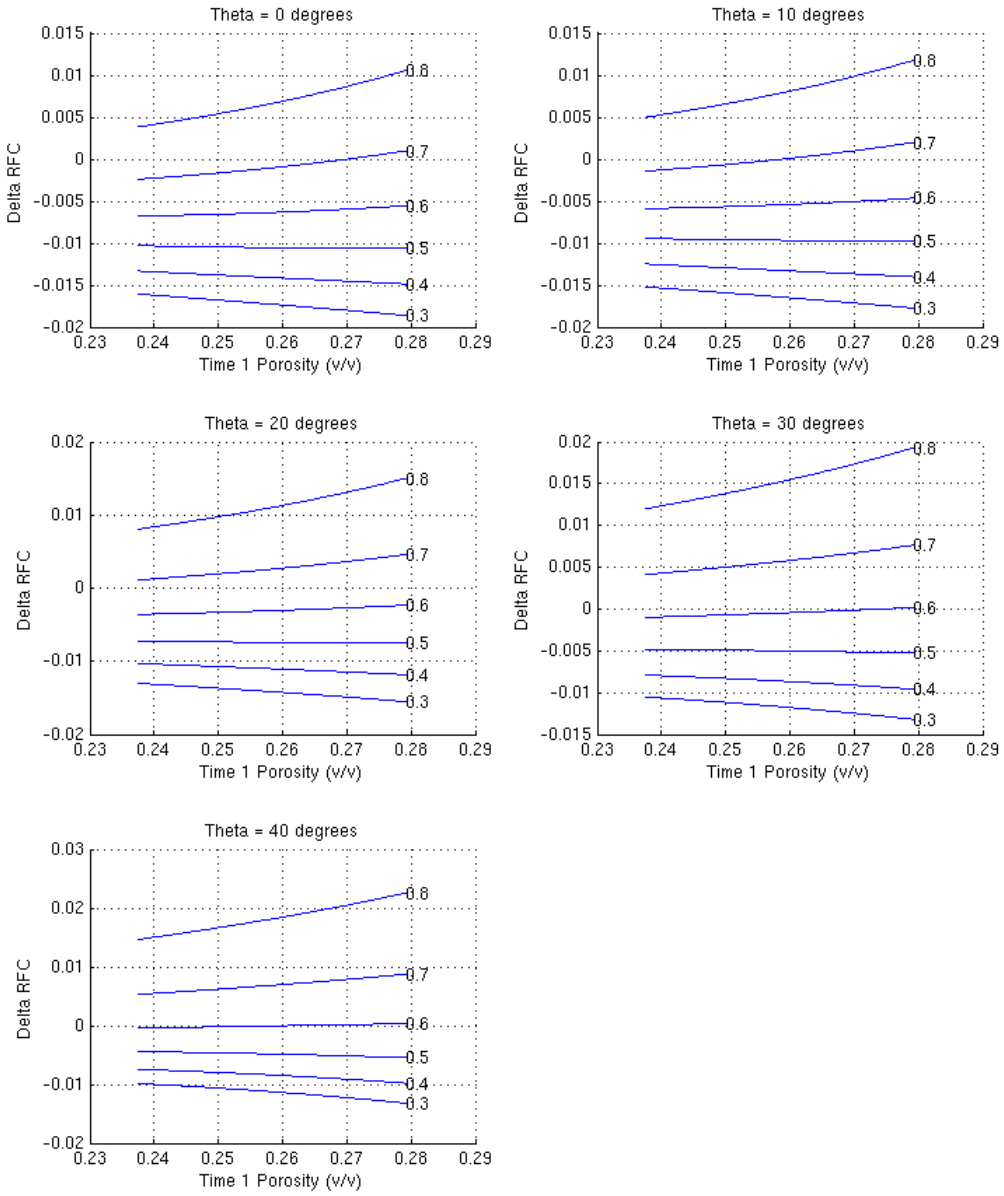

Figure D-3: Change in reflection coefficient versus angle between the T_1 depleted and compressed reservoir and the T_2 water flooded reservoir with labeled T_2 water saturations.

Vita

Christy Finch Gautre was born in New Orleans, Louisiana and received her B.S. in Mathematics from Centenary College of Louisiana in Shreveport in 2002. She worked as a Physical Scientist at the Naval Oceanographic Office at Stennis Space Center in Mississippi from 2002 until 2007. She is currently employed as a Senior Geoscience Technician at the Shell Exploration and Production Company in New Orleans, Louisiana, where she began working in 2007. She formally enrolled as a degree-seeking student at the University of New Orleans in 2007 after taking several courses at the University between 2003 and 2006.